Wind, waves, and acoustic background levels at Station ALOHA

Fred K. Duennebier,[1] Roger Lukas,[2] Eva-Marie Nosal,[3] Jérome Aucan,[4] and Robert A. Weller[5]

Received 4 May 2011; revised 29 December 2011; accepted 3 January 2012; published 10 March 2012.

[1] Frequency spectra from deep-ocean near-bottom acoustic measurements obtained contemporaneously with wind, wave, and seismic data are described and used to determine the correlations among these data and to discuss possible causal relationships. Microseism energy appears to originate in four distinct regions relative to the hydrophone: wind waves above the sensors contribute microseism energy observed on the ocean floor; a fraction of this local wave energy propagates as seismic waves laterally, and provides a spatially integrated contribution to microseisms observed both in the ocean and on land; waves in storms generate microseism energy in deep water that travels as seismic waves to the sensor; and waves reflected from shorelines provide opposing waves that add to the microseism energy. Correlations of local wind speed with acoustic and seismic spectral time series suggest that the local Longuet-Higgins mechanism is visible in the acoustic spectrum from about 0.4 Hz to 80 Hz. Wind speed and acoustic levels at the hydrophone are poorly correlated below 0.4 Hz, implying that the microseism energy below 0.4 Hz is not typically generated by local winds. Correlation of ocean floor acoustic energy with seismic spectra from Oahu and with wave spectra near Oahu imply that wave reflections from Hawaiian coasts, wave interactions in the deep ocean near Hawaii, and storms far from Hawaii contribute energy to the seismic and acoustic spectra below 0.4 Hz. Wavefield directionality strongly influences the acoustic spectrum at frequencies below about 2 Hz, above which the acoustic levels imply near-isotropic surface wave directionality.

Citation: Duennebier, F. K., R. Lukas, E.-M. Nosal, J. Aucan, and R. A. Weller (2012), Wind, waves, and acoustic background levels at Station ALOHA, *J. Geophys. Res.*, *117*, C03017, doi:10.1029/2011JC007267.

1. Introduction

[2] The interaction of wind with the ocean surface generates sound that dominates the background acoustic spectrum at the deep-ocean floor from 0.05 Hz to more than 6 kHz. There are several energy transfer processes involved: wind-to-wave, wave-to-acoustic, and acoustic-to-seismic. Simultaneous measurements of wind, wave, acoustic and seismic signals in one location and in the same frequency band for an extended period are rare, and thus models of these transfer processes are poorly constrained.

[3] Many papers have been written concerning the sources of low-frequency acoustic background (0.05–50 Hz) in the ocean [*Hasselmann*, 1963; *Webb and Cox*, 1986; *Babcock et al.*, 1994; *Webb*, 2007; *Farrell and Munk*, 2008; *Munk*, 2009; *Dahm et al.*, 2006; *Kedar et al.*, 2008; *Chi et al.*, 2010; *Ardhuin et al.*, 2011] and, while all studies conclude that wave energy is the major source of this acoustic energy, there is uncertainty as to how and where the wave energy is transmitted to the deep ocean. At frequencies above 100 Hz air bubbles and direct pressure from turbulence and breaking waves are known to generate sound that correlates with wind speed [*Kerman*, 1984; *Ma et al.*, 2005; *Gaul et al.*, 2007], but there is considerable uncertainty as to the origin of the wind-related noise at frequencies below 100 Hz. Wavelengths at low frequencies in relatively shallow water are long enough that direct pressure from the variation in the ocean surface elevation supplies energy to the ocean floor, for example, tides, tsunami, and infragravity waves in the deep ocean, and single-frequency microseisms in shallow water [*Bromirski*, 2009]. The relative minimum in the ocean wave energy spectrum near 0.07 Hz, between the infragravity wave region [*Webb*, 2007] and the wind-driven wave energy spectrum, leads to a "hole" in the acoustic spectrum. The ocean acoustic spectrum is similar to the wave energy spectrum at frequencies above 0.07 Hz [*Bromirski et al.*, 1999], with a strong tendency for correlation between ocean wave energy and acoustic energy at twice the frequency of the waves [*Kibblewhite and Wu*, 1991; *Webb and Cox*, 1986;

[1]Department of Geology and Geophysics, SOEST, University of Hawai'i at Mānoa, Honolulu, Hawaii, USA.
[2]Department of Oceanography, SOEST, University of Hawai'i at Mānoa, Honolulu, Hawaii, USA.
[3]Department of Ocean Resources and Engineering, SOEST, University of Hawai'i at Mānoa, Honolulu, Hawaii, USA.
[4]Laboratoire d'Etudes en Géophysique et Océanographie Spatiale, Institut de Recherche pour le Développement, Toulouse, France.
[5]Woods Hole Oceanographic Institution, Woods Hole, Massachusetts, USA.

0148-0227/12/2011JC007267

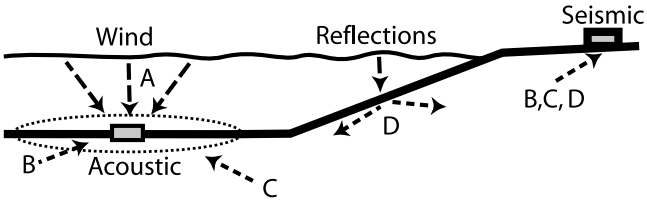

Figure 1. Schematic of possible acoustic energy sources. The letter A indicates L-H pressure from above the sensor, the letter B indicates seismic energy generated in the region in the vicinity of the sensor, the letter C indicates energy generated at the site of distant storms, and the letter D indicates energy generated by reflections at shorelines.

Kedar et al., 2008]. The ubiquitous "microseism peak" near 0.175 Hz, observed globally in seismic and infrasound records [*Garcés et al.*, 2003], is correlated with the peak of the ocean wave energy spectrum.

[4] The accepted mechanism for low frequency sound generation by ocean waves is the nonlinear double-frequency wave-wave mechanism described by *Longuet-Higgins* [1950] and expanded on by many others. The Longuet-Higgins (L-H) theory predicts that the constructive interference of ocean surface waves traveling in opposing directions having nearly the same wave number generates acoustic energy that propagates nearly unattenuated to the deep-ocean floor at twice the frequency of the generating waves [*Longuet-Higgins*, 1950; *Hasselmann*, 1963; *Kibblewhite and Wu*, 1991; *Cato*, 1991]. The amplitude of the resulting acoustic signal (hereafter L-H pressure) is proportional to the product of the elevations of the opposing wave components; thus, to predict the level of sound generated one must know both the frequency spectrum of the waves and their directionality. A fraction of the L-H pressure with wave numbers appropriate for coupling to seismic waves can propagate laterally, providing a surface-integrated source for microseism energy observed at large distances from the point of generation. Attenuation characteristics of both the ocean waves and the seismic waves imply that low frequencies will be observed at greater distances than high frequencies. Adding to the complexity, the reflectivity of shorelines is also frequency-dependent with reflectivity larger at low frequencies and reflectivity likely decreasing with increasing wave amplitude as wave breaking absorbs energy [*Elgar et al.*, 1994; *Ardhuin et al.*, 2011].

[5] Observations of seismo-acoustic energy at twice the frequency of ocean waves are well documented, particularly at seismic stations near coasts and by marine acoustic studies [*Sutton and Barstow*, 1990; *Bromirski et al.*, 1999; *Cessaro*, 1994; *Babcock et al.*, 1994; *Kedar et al.*, 2008; *Chi et al.*, 2010]. *Zhang et al.* [2010] used seismic array data to backtrack high-amplitude seismic wave trains to ocean sources, and *Webb and Schultz* [1992] used Arctic Ocean bottom data to determine the direction to sources of microseisms. *Bromirski et al.* [2005] and *Chi et al.* [2010] observed that the microseism signal associated with large storms increases as storms approach shorelines from the deep ocean. One such storm generated a microseism signal detected by seismometers in California when it reached the Hawaiian coast [*Bromirski et al.*, 2005]. At frequencies below 0.35 Hz, microseisms from storms at global distances are detected at seismic stations [*Zhang et al.*, 2010]. A likely scenario could be that seas within a storm generate microseisms that are detected by distant seismo-acoustic sensors almost immediately, while swell generated by the storm impacts a distant shoreline days later, generating seismo-acoustic energy that is also detected by sensors that are distant from both the storm and the shoreline. In this case, the wind conditions in the vicinity of the sensor are expected to be uncorrelated with acoustic levels.

[6] Based on previous studies, there are at least four possible energy paths for microseismic energy shown as a cartoon in Figure 1: the letter A indicates local wind wave-generated L-H pressure above the hydrophone, the letter B indicates seismic waves generated by L-H pressure in the region surrounding the sensor, the letter C indicates seismic waves generated by L-H pressure at sites of distant storms, and the letter D indicates seismic waves generated by reflection of waves from shorelines. Seismometers on land are not sensitive to A, since there is no water above the sensor, but the signal observed at hydrophones will be some combination of all four sources.

[7] A few data sets have been obtained with collocated acoustic and atmospheric measurements, but most suffer from sensor locations on land or in shallow water, inadequate instrumentation, short wind fetch, short record length, or consideration of only the frequency band near the energy peak [*Kibblewhite and Wu*, 1991; *Babcock et al.*, 1994; *Wilcock et al.*, 1999]. *McCreery et al.* [1993] made multi-year acoustic observations at deep bottom-mounted hydrophones near Wake Island that were correlated with wind speeds measured at Wake Island and SOWM (Spectral Ocean Wave Model) wave hindcasts [*Pierson*, 1982]. *McCreery et al.* [1993] observed saturation of the acoustic spectrum between 1 and 8 Hz, termed the HOLU spectrum, similar to the saturation of the ocean wave energy spectrum described by *Phillips* [1985]. Below 0.3 Hz, the acoustic energy at the Wake Island hydrophones correlated with the wave energy at half the acoustic frequency as expected for the Longuet-Higgins theory. However, acoustic energy above 0.3 Hz was most strongly correlated with model wave energy at about one fifth the acoustic frequency. This issue will be discussed in a later section.

2. Data

[8] In this study, we use a 20-month time series of ocean floor acoustic signals, ocean surface wind speed, wave spectra, and seismic data to study the sources of the acoustic energy observed and the mechanisms whereby it is transmitted to the ocean floor and into the earth, and some aspects of directionality of wind waves. We will use the term "wind waves" and "wave energy" when referring to ocean surface waves generated by wind, not to be confused with seismic surface waves or internal waves. While the acoustic data extend to 10 kHz in frequency, we restrict detailed discussion to signals at frequencies below 100 Hz. The locations of the acoustic, wind, wave, and seismic sensors are shown in Figure 2.

2.1. Acoustic Data

[9] The acoustic time series was obtained from a broadband hydrophone at the ALOHA Cabled Observatory

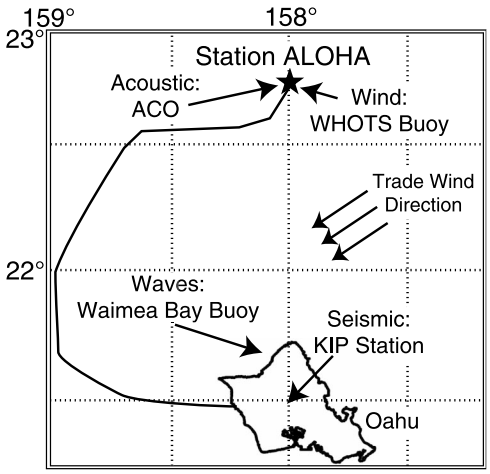

Figure 2. Instrumentation map. Data used in this study include ocean floor acoustic data from the ALOHA Cabled Observatory (ACO) at Station ALOHA, wind speed from the WHOTS buoy at Station ALOHA, wave spectra from the Waimea Bay Buoy, and vertical seismic data from the KIP seismic station on Oahu, Hawaii.

(ACO) at Station ALOHA [*Karl and Lukas*, 1996], 100 km north of Oahu, Hawaii. The broadband hydrophone (OAS Model E-2PD) was suspended 10 m above the ocean floor in 4720 m of water as part of a proof-of-concept package when the ACO was emplaced at Station ALOHA in February 2007 [*Duennebier et al.*, 2008]. Continuous 24-bit data were sampled at 96 kHz with ambient noise level observable from 0.02 Hz to 6 kHz. The analog hydrophone data were pre-whitened prior to digitization using a twin-T filter in the preamplifier (Appendix A) to minimize the microseism peak [*Duennebier et al.*, 2002]. The resulting 40 dB compression allowed resolution of the complete 150 dB signal in the available 144 dB digital dynamic range. Data were transmitted over the retired HAW-4 electro-optical commercial telecommunications cable to the AT&T Makaha Cable Station on Oahu where they were decimated to 24 kHz sample rate, and transmitted to the University of Hawaii-Manoa for archival. Nearly continuous data were collected for 20 months until the package was removed in October 2008. The observatory was re-installed in June 2011, and is again collecting data.

2.2. Wind Data

[10] The WHOTS meteorological buoy [*Plueddemann et al.*, 2006], with ASIMET instrumentation [*Colbo and Weller*, 2009], is located about 10 km (2 water depths) from the ACO. Data are collected in 1-min boxcar averages that are further averaged into hourly samples that are available online from the Woods Hole Oceanographic Institution at the Upper Ocean Processes Group data site (R. Weller, Project WHOTS–WHOI Hawaii Ocean Time-series Station, Woods Hole Oceanographic Institution, 2009, available at http://uop.whoi.edu/projects/WHOTS/whotsdata.htm).
Hourly averaged wind speed data at a height of 2.7 m above sea level are processed by the WHOTS team into U_{10}, the wind speed at an elevation of 10 m, and u^*, the friction velocity, providing key data for this paper. Wind direction, wind stress, and other variables are also available at the same Web site but were not used in this study.

2.3. Wave Data

[11] Wave spectra were obtained from a buoy outside of Waimea Bay, Oahu. The buoy used in this study is a spherical, 0.9 m diameter, mkII directional Waverider, deployed and maintained by the University of Hawaii Sea Level Center [*Aucan*, 2006; M. Merrifield, HiOOS assets, Hawaii Ocean Observing System, Honolulu, 2009, available at http://www.soest.hawaii.edu/hioos/data_product/assets.php]. The buoy hull contains a heave-pitch-roll sensor, a three-axis compass and horizontal accelerometers sampled at 1.28 Hz. The complete directional spectrum is transmitted to shore via a HF radio transmitter and archived under station ID 106 by the Coastal Data Information Program (CDIP), at the Scripps Institution of Oceanography. Pre-processed half-hourly samples from the SIO CDIP data center were averaged into hourly spectral samples up to 0.5 Hz for this study. Data from other buoys in the Hawaiian region are also available, but the Waimea Buoy is the closest to ACO.

2.4. Seismic Data

[12] Short period vertical (channel BHZ) seismic motion data from the KIP seismic station were obtained from IRIS (Incorporated Research Institutions for Seismology) (U.S. Geological Survey, seismic station IU KIP, 2009, available at http://earthquake.usgs.gov/monitoring/operations/station.php?network=IU&station=KIP) for the 20-month observation period, and hourly spectra were calculated for comparison with the acoustic and wave spectral time series. The 20 Hz sample rate vertical BHZ data were high pass filtered at 0.05 Hz. 17-min, 2048-sample spectra were generated and subsequently averaged into hourly values.

3. Analyses

[13] Spectral time series of the ACO acoustic data are compared with the wind speed time series, and with the wave and seismic spectral time series to understand the relationships among these data sets. Previously published models for the wind-to-wave and wave-to-bottom pressure transfer functions are used to estimate the L-H pressure available at the ocean floor observed at the hydrophone and available to propagate laterally as seismic waves. The validity of several assumptions that were required to make these conversions is tested by comparison of the various data sets, and empirical modifications of the models are suggested to better fit the data.

3.1. The Acoustic Spectral Time Series

[14] A 2^{21} point (1.5-min) Hanning-windowed time sample of 24 kHz ACO acoustic data was taken every 5 min to provide power spectral densities of the acoustic data in a 20-octave band from 0.0114 Hz to 10 kHz. 476 log-spaced estimates with 100 estimates per decade above 0.6 Hz were selected from the 10^6 linearly spaced spectral estimates provided by the FFT. Samples below 0.6 Hz are linearly spaced in frequency to preserve resolution at low frequencies. The 12 spectra obtained each hour were averaged to provide the

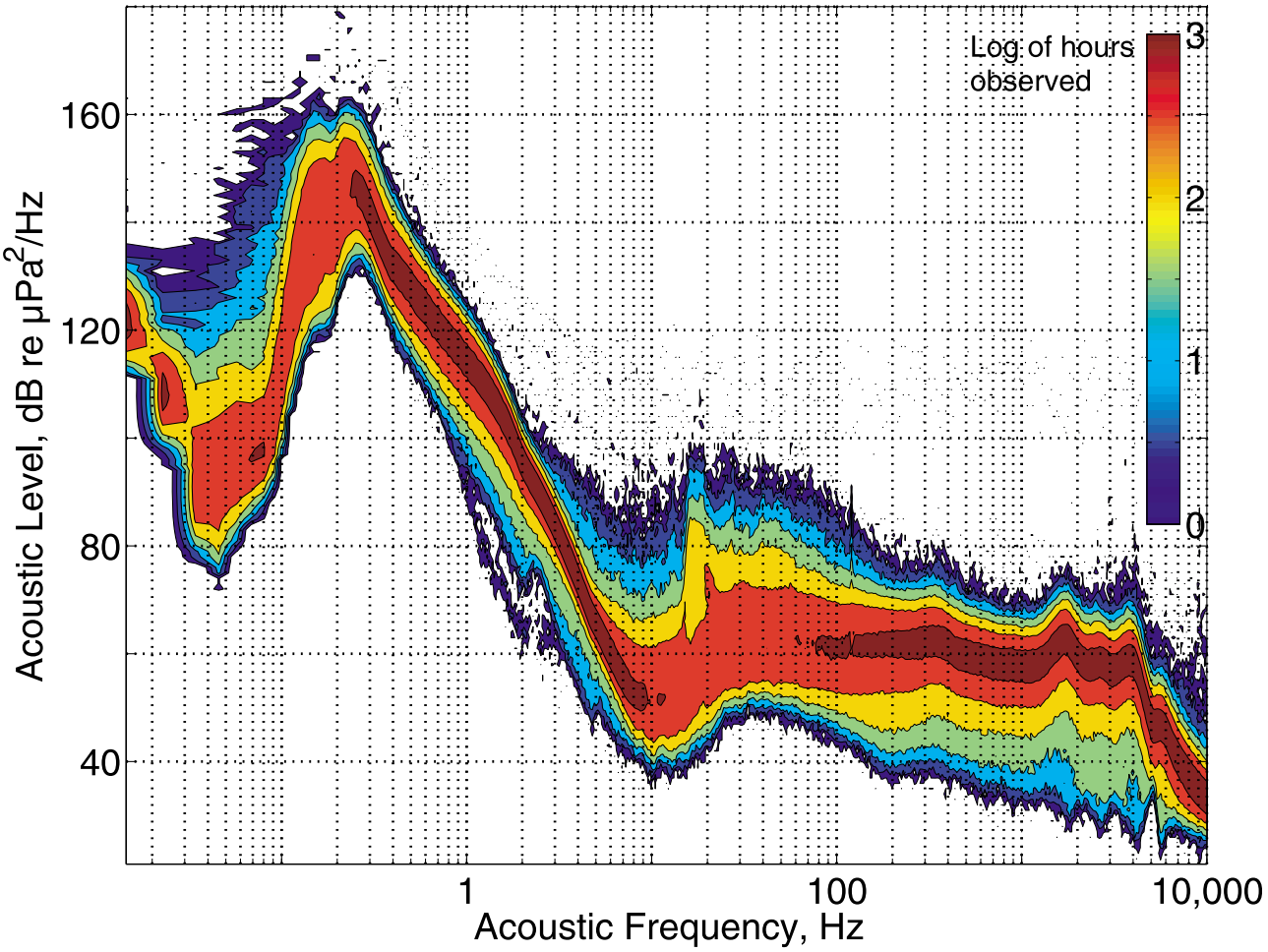

Figure 3. Occurrences of spectral levels for all hourly acoustic data from 0.0145 Hz to 10 kHz. Colors represent the log of the number of hours at each level observed at each frequency.

hourly spectra used in this study. All data displayed have been corrected for the instrument response as modified for this study to remove narrow-band stationary oscillations as explained in Appendix A.

[15] The acoustic data span almost 6 decades in frequency and more than 150 dB in energy level. The sample density (log of the number of hourly samples at each frequency within 1 dB energy level bins) is contoured in Figure 3. The highest energy levels are observed at the microseism peak near 0.175 Hz. The apparent double peak between 0.1 and 0.2 Hz may be an artifact resulting from uncertainty in the response of the pre-whitening filter (Appendix A). Note the generally narrow range of spectral values between 2 and 6 Hz compared to other frequency bands. A sharp increase in the range of spectral levels near 16–22 Hz is associated with blue and fin whale vocalizations common in winter months [*Diachok and Duennebier*, 2010]. Other transient signals are associated with earthquakes, shipping, and biological sources. Resonances above 2 kHz are the result of the physical size of the sensor being close to the acoustic wavelengths (see Appendix A). The ambient background level is above instrument noise level from below 0.02 Hz to about 4 kHz, where the system noise floor is roughly 30 dB re μPa^2/Hz.

3.2. Correlation of the Acoustic Spectra With Wind Speed

3.2.1. Processing Methods

[16] Each frequency of the ACO acoustic spectral time series was correlated with the wind speed time series over the entire 20 months (14,720 h), accounting for gaps in the recordings by replacing missing values with the mean values of surrounding samples. The ACO data have 14,391 spectra with the longest gap being 100 h. The WHOTS wind data have 14,598 hourly averages with the longest gap being 26 h. Figure 4 shows the maximum correlation coefficient (r) between wind speed and acoustic level at each frequency, and the lag where r is maximum.

3.2.2. Local Wind Speed-Acoustic Correlation Characteristics

[17] The characteristics of the correlation between the local wind speed and the acoustic spectral time series over the entire 20-month period constrain the sources of the acoustic background. The low r-value below 0.4 Hz implies that local winds typically do not supply the energy observed in the most energetic part of the acoustic spectrum, including the microseism peak. At higher frequencies there are only two bands, 2.2–6 Hz, and 15–130 Hz, where $r < 0.5$, (less than 25% of the variance explained by changes in wind

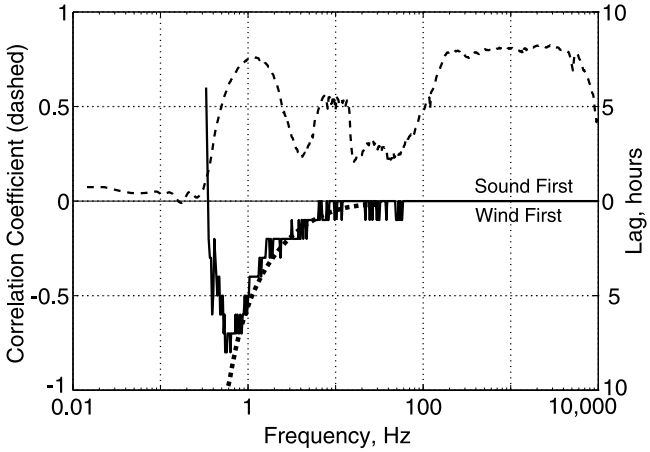

Figure 4. ACO acoustic energy correlation with wind speed. The dashed curve shows the maximum correlation coefficient within a ±20 h region around zero lag. The solid curve shows the lag in hours at maximum correlation. The dotted line is a theoretical estimate of expected lag for growing seas (see text for explanation).

speed). Between 2.2 and 6 Hz the acoustic levels change little with wind speed variations at the predominant wind speeds, leading to low *r*-values, and in the upper band between 15 and 100 Hz biological and shipping noise dominate the spectra. *r*-values rise to ~0.8 above 100 Hz, remaining high up to 5 kHz.

[18] The lag between the wind and acoustic level at maximum correlation decreases roughly exponentially from about 7 h (wind leading) near 0.6 Hz to less than an hour for $f > 6$ Hz. The dotted lag line in Figure 4 is an estimate of the time required for the wave spectrum to reach equilibrium when up-fetch wind speed increases instantaneously from zero to an arbitrarily high wind speed, assuming that 5,000 wavelengths are required to reach equilibrium [*Pierson and Moskowitz*, 1964]. The observed lag and *r*-values strongly imply that local wind-driven seas are responsible for much of the observed acoustic energy above 0.4 Hz. The lack of an appreciable lag above 10 Hz implies that much of the observed acoustic energy above 10 Hz is generated within a few km of the observatory. Similar correlations and lags of ocean bottom seismic signals with wind speed were reported by *Wilcock et al.* [1999].

3.2.3. Sorting Acoustic Data by Wind Speed

[19] The hourly averaged acoustic spectra were sorted by wind speed (U_{10}, the wind speed at 10 m above sea level) into 0.5 m/s bins (Figures 5 and 6) from 0 to 0.5 m/s, 0.5 to 1 m/s, etc. There were fewer than 12 h when wind speed was observed above 12.5 m/s (Figure 5), and, although displayed in Figures 6–10, 12–14, and 17, the levels associated with wind speeds higher than 12.5 m/s are less certain than those at lower wind speeds. Northeast trade winds at Station ALOHA often blow for days at a time at speeds between 6 and 11 m/s, resulting in seas nearly in equilibrium with the wind. The time intervals when low and high wind speeds were observed are short in duration, thus, it is likely that the wavefield was not in equilibrium with the wind during those times, resulting in lower than expected acoustic levels at high wind speeds and higher than expected levels at low wind speeds, particularly at frequencies between 0.4 and 10 Hz.

[20] Hourly acoustic spectral data obtained over the 20-month sample period were sorted by local wind speed, and the distributions of acoustic levels at each wind speed were examined to obtain a representative background acoustic level for each frequency and wind speed. The resulting spectral distributions (not shown) generally have a positive skew and large kurtosis in spectral regions where contributions from non-wind related signals are rare and where the correlation with local wind speed is high - roughly at wind speeds from 3.5 to 10.5 m/s and frequencies from 1 to 10 Hz and above 100 Hz. As shown by other studies [e.g., *Gaul et al.*, 2007], the acoustic levels are often biased to higher values by transient sources such as shipping, marine mammal vocalizations, and earthquakes. In frequency bands where such extraneous signals are more common and where the signal generated by the local wind is small relative to other sources the distributions are flattened (low kurtosis), and display smaller skew. Spectral distributions at 0–1 m/s local wind speed are roughly normally distributed, indicating random acoustic levels caused by extraneous signals only. As wind speed increases, skew becomes more positive and kurtosis increases as the levels become better correlated with wind speed. To get a stable and robust estimate of the levels appropriate for a particular wind speed, we need to avoid spectral samples where extraneous signals are present.

[21] Other researchers have removed spectra that appeared to have anomalously high levels [e.g., *Gaul et al.*, 2007]. Instead, we use the level bounding the lowest octile of the distribution at each frequency, where levels are lower only 1/8th of the time at each frequency. This effectively eliminates data contaminated by transients and yet the levels are not influenced by anomalously low values. This selection process removes subjectivity and allows an independent selection for each frequency and wind speed, removing the effects of extraneous signals except where they are present more than 7/8ths of the time. The resulting estimates (Figure 6) are generally <3 dB lower than median levels when wind speeds are 5 m/s or greater; below 0.3 Hz and

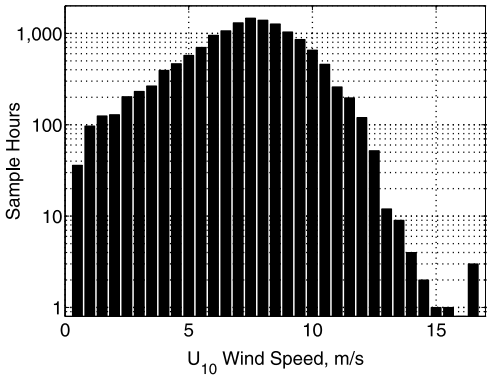

Figure 5. WHOTS buoy U_{10} wind speed distribution for the period February 2007–October 2008 at Station ALOHA. The number of hours recorded in each wind speed interval is plotted. Half of the samples occur between 5.75 and 8.5 m/s. Note that there are only 7 h during the 20 months of recording when the average wind speed was greater than 14 m/s.

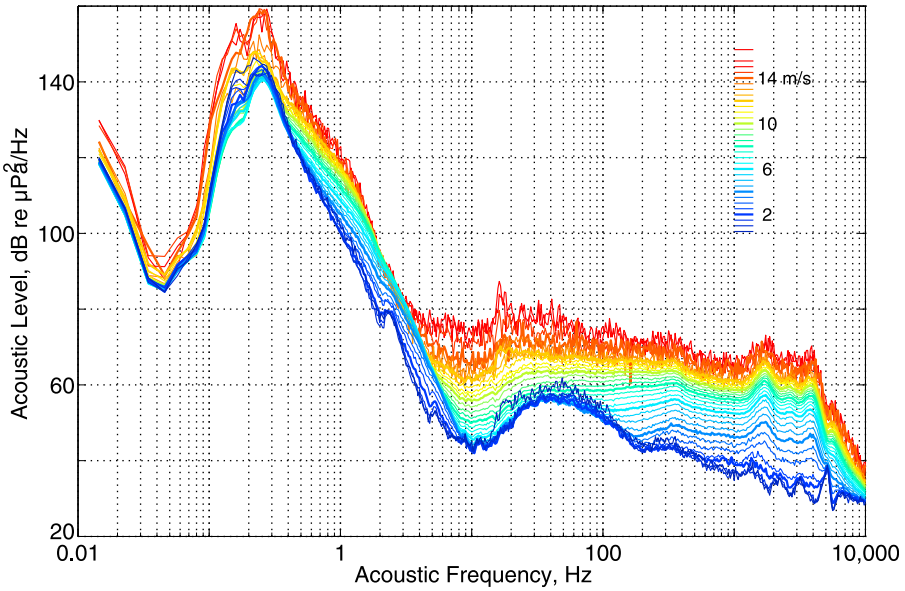

Figure 6. ACO acoustic spectra sorted by U_{10} wind speed. Spectra are plotted by color in 0.5 m/s wind speed steps from zero (dark blue) to 16.5 m/s (red) with heavy lines every 2 m/s (no data at 16 m/s).

from 10 to 40 Hz they can be 5–12 dB lower than median levels. These spectra are displayed and compared with model results in Figures 6–10, 12–14, and 17.

[22] Higher acoustic levels are generally associated with higher wind speeds, as shown in Figure 6. The maximum range of acoustic levels with wind speed (about 30 dB between wind speeds of 1 and 15 m/s) is observed near 2–4 kHz. The variation of acoustic level with wind speed is largest near 10 Hz at wind speeds between 7 and 15 m/s, changing at a rate of about 4 dB/m/s. Noise unrelated to the local wind puts a floor under acoustic levels at lower wind speeds. Detailed analysis of noise levels between 50 and 500 Hz recorded in 1975 by *Gaul et al.* [2007] shows a strong correlation with wind speeds that is limited by shipping noise at wind speeds below 2.5 m/s. Their analysis yields acoustic levels that are within 2 dB of those presented here near 500 Hz, but their noise floor is lower at low wind speeds. This difference may be the result of their detailed selection for times when local shipping is absent, while the data presented here have not been specifically selected to exclude such transients.

3.2.4. "Rotated" Spectra

[23] A term (10 n $\log_{10} f$, where n = 8), was added to the spectral values shown in Figure 6 and plotted in Figure 7 to

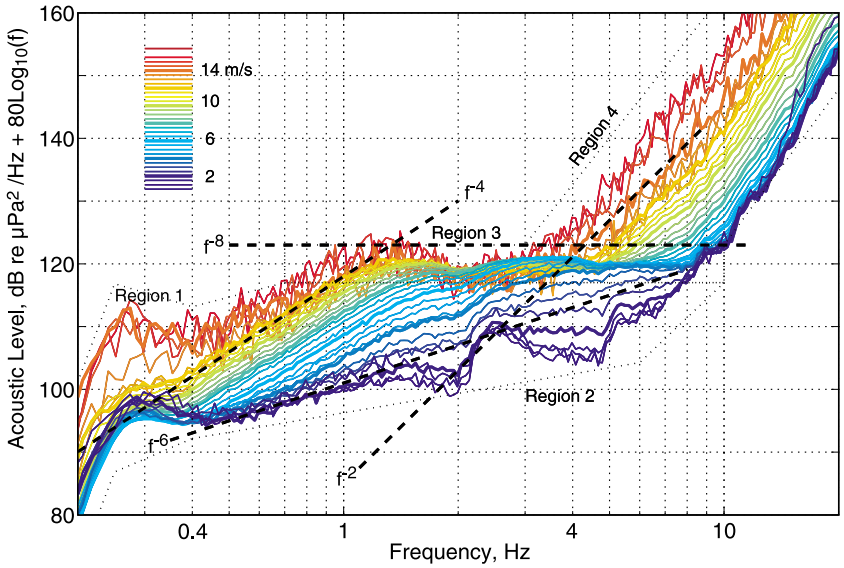

Figure 7. "Rotated" acoustic spectra as a function of wind speed (see text for explanation). Each line represents a different wind speed in 0.5 m/s steps from U_{10} = 0.5 (dark blue) to 16.5 (red) m/s with heavy lines every 2 m/s (no data at 16 m/s). Black dashed lines indicate prominent spectral slopes, and dotted boxes outline regions discussed in 3.2.5.

improve visualization of variations with wind speed, emphasizing the saturation level apparent between 1.5 and 8 Hz. The addition of this term effectively "rotates" the spectrum counterclockwise by $3n$ dB/oct, thus, the $n = 8$ value rotates the spectrum counterclockwise by 24 dB/oct, and flattens regions where the slope of the spectrum is f^{-8}. Although the average slope across the observed spectrum is roughly f^{-4}, (-12 dB/oct) a considerable amount of wind-related structure in the acoustic spectrum is evident. Narrow-band ± 2 dB variations in the spectra that are stationary and independent of wind speed, possibly caused by seismo-acoustic interactions with the ocean sediments [*Kibblewhite and Wu*, 1996; *Stephen et al.*, 2007], have been removed for this study using the method shown in Appendix A.

3.2.5. Regions of the Acoustic Spectrum

[24] Four spectral regions are delineated in Figure 7 and in Figures 8, 9, 10b, and 14: R1 (Region 1): the uncorrelated region below 0.4 Hz; R2: the f^{-4} to f^{-6} slope region; R3: the f^{-8} slope saturated region, and R4: the f^{-2} slope region. In R1 the spectral levels show little correlation with local wind speed at speeds below 11 m/s, even though the peak of the acoustic energy spectrum (microseism peak) occurs in this region (Figure 3). R2 is characterized by observed spectral slopes of f^{-4} below $\sim$1.5 Hz increasing to f^{-6} at higher frequencies. In R3 the spectral levels are relatively constant for $U_{10} > 4$ m/s with a slope of f^{-8}. This "saturation" level, where the acoustic level is nearly independent of wind speed, was termed the HOLU spectrum by *McCreery* [1992]. The levels droop below the f^{-8} level near 2 Hz at higher wind speeds such that there is a negative correlation of the acoustic level with wind speed, as also observed by *McCreery et al.* [1993] and *Wilcock et al.* [1999]. At the boundary between R3 and R4 the spectral slope changes abruptly from f^{-8} to $\sim f^{-2}$ at frequencies that decrease with increasing wind speed. Consider, for example, the acoustic levels at a frequency of 5 Hz as wind speed increases; the level rises in R2 until the wind speed reaches 4 m/s, the level then stays constant in R3 up to wind speeds of 10 m/s, and then rises again with wind speed in R4. The signals in R4 are the "booms" and those in R2 are the "busts" in *Farrell and Munk* [2010].

3.3. Correlation With Waves

[25] While Figures 4–7 clearly show how wind speed correlates with the ACO acoustic energy levels, the pathways that wind energy takes to the hydrophone are not obvious. The transfer of wind energy into ocean floor acoustic energy involves (at least) four parts: 1) the transfer of energy from wind to waves, 2) from waves to depth-independent pressure fluctuations in the ocean (L-H pressure), 3) modification of the pressure fluctuations by the ocean floor, and 4) propagation of the energy at and below the ocean floor as seismo-acoustic waves. At this point, we apply previously derived theoretical and experimental estimates of the wind-to-wave and wave-to-acoustic energy transfer functions to model the L-H pressure, ignoring lateral propagation of the seismic energy until later in the paper. We could eliminate the wind-to-wave transfer function if appropriate directional wave spectra were available at ACO, but the closest wave buoy (Waimea Bay) is more than 100 km distant and is shadowed from the east and south by the island of Oahu, blocking at least part of the trade wind fetch from the buoy (Figure 2). Also, this and similar wave measurement buoys are unable to detect wave motions at frequencies above 0.5 Hz. We use the Waimea Bay wave data later in this paper, but for the present analysis we will utilize model wave energy spectra.

3.4. Wave Model

[26] Open-ocean surface wave energy spectra depend on a number of factors including wind speed and direction, fetch, duration of the wind, surface tension, wave breaking, and presence of swell. Since correlations of the bottom acoustic fluctuations with wind speed are observed in the data, independent of other parameters, we make several model assumptions that eliminate dependence of the wave spectrum on parameters other than wind speed.

[27] Initially, we assume that all of the energy reaching the ocean floor at ACO is the result of only the local wind-driven waves, ignoring lateral propagation of energy along the ocean floor until later. The bottom depth at ACO is much larger than the 800 m required for 25-s period waves to have significant interaction with the bottom, thus we ignore direct pressure on the bottom. We assume that spectral modifications resulting from bottom interactions are independent of changes in acoustic level, and can thus be included in the instrument response (Appendix A). We initially assume that the seas are isotropic, with waves traveling in all directions with equal amplitudes. The Longuet-Higgins mechanism, assumed to be responsible for the energy in the acoustic spectrum below about 100 Hz, puts ocean wave energy into the deep ocean at twice the frequency of the ocean surface waves with amplitude proportional to the product of the amplitudes of the opposing waves [*Longuet-Higgins*, 1950; *Kibblewhite and Wu*, 1991]. At low wind speeds and at higher frequencies, the source of acoustic variations transitions to purely acoustic mechanisms generated by turbulence, biology, shipping, and other energy sources [*Gaul et al.*, 2007]. While each of these assumptions is certainly incorrect for some frequencies and under some conditions, they provide a convenient starting point for development of a null hypothesis model for the observed signals.

[28] We follow the lead of *Farrell and Munk* [2010] and divide the wave spectrum into two regions, gravity waves at low frequencies, and ultra-gravity waves at higher frequencies. *Phillips* [1958] hypothesized equilibrium between wind energy input and dissipation of gravity waves for wave numbers larger than the peak of the elevation energy spectrum, implying spectral saturation under equilibrium conditions, where the energy levels do not increase with increasing wind stress. *Pierson and Moskowitz* [1964] (hereafter P-M) extended the Phillips spectrum to include wave numbers near and below the peak, outside of the equilibrium range. The P-M equilibrium balances wind energy input, wave energy dissipation, and spectral energy divergence from nonlinear wave interactions. In using these model spectra, we implicitly assume that the wind has the same speed and direction over a distance upwind of the observatory that is long enough for the seas to reach equilibrium with the wind above the observatory. For the P-M spectrum, this requires a fetch of at least 5,000 wavelengths, or about 500 km for 8-s waves at the peak of the trade wind wave spectrum, 8 km for 1-Hz waves,

and 330 m for 5-Hz waves (based on the group velocity being half the phase velocity, $c_g = \omega/2\kappa$) [*Pierson and Moskowitz*, 1964]. Deviations from this equilibrium assumption are seen in Figure 4, where the acoustic spectral levels lag wind speed changes by about 7 h near 0.3 Hz wave frequency (0.6 Hz acoustic frequency) decreasing to less than an hour near 5 Hz wave frequency. In general, we observe lower than expected acoustic spectral levels when wind speed is increasing and higher than expected when wind speed is decreasing. If this deficit in level when wind speed is increasing is the same as the excess when the wind is decreasing, then the observed spectral level will approximate the expected equilibrium level except at high wind speeds, since the duration of high wind speed events is too short for equilibrium to be reached.

[29] Some of the important limitations of the P-M spectrum are that it:

1) includes only weak nonlinearity; no energy transformation occurs across wave numbers through wave-breaking, and nonlinear wave-wave interactions are not treated explicitly;

2) assumes an unlimited fetch (addressed by the JONSWAP spectrum [*Hasselmann et al.*, 1973]);

3) assumes ultra-gravity waves are part of the equilibrium range [*Phillips*, 1985];

4) doesn't include the effects of surface tension (capillary waves);

5) doesn't include advective effects where shorter waves are Doppler shifted by motions of longer waves or due to mean flows;

6) doesn't consider feedback of waves to the wind stress;

7) is omnidirectional (i.e., it doesn't address the directional spectrum).

[30] Despite the limitations, we begin with the P-M model as the basis for the surface wave spectrum since it can be specified from the available wind speed data. Modifications to the model that provide better agreement between data sets will be discussed as they are introduced, including the effects of directionality of the wavefield and the contributions of ultra-gravity waves.

[31] Of the many choices for wave models, [e.g., *Elfouhaily et al.*, 1997; *Alves et al.*, 2003; *Donelan et al.*, 1985], we choose to begin with the P-M model as formulated by *Alves et al.* [2003] based on the original P-M data. We do not use the JONSWAP model spectrum [*Hasselmann et al.*, 1973] since it includes terms for varying fetch, assumed to be unlimited in this study, and because it does not exhibit saturation characteristics discussed below. In terms of wave number, using notation suggested by W. E. Farrell (personal communication, 2009) and used by *Farrell and Munk* [2008], the wave elevation energy spectrum model is given by:

$$\langle \varsigma^2 \rangle = \iint \kappa F_\varsigma(\kappa) H(\kappa,\theta) d\theta d\kappa, \quad \int_{-\pi}^{\pi} H(\kappa,\theta) d\theta = 1 \qquad (1)$$

where $\langle \varsigma^2 \rangle$ is the mean squared wave elevation spectrum, $\kappa = 2\pi/\lambda$, is the wave number, λ is the wavelength, F_ς is the elevation energy spectrum, H is the wave directionality function, and θ is the angle from the downwind direction. The P-M wave spectrum, developed for wind speed at an elevation of 19.5 m, was updated by *Alves et al.* [2003] for the wind speed at an elevation of 10 m, (U_{10}):

$$S(f_\varsigma) = 0.00952 g^2 (2\pi)^{-4} f_\varsigma^{-5} \exp\left[-1.25\left(\frac{f_p}{f_\varsigma}\right)^4\right] \qquad (2)$$

where S is the wave elevation frequency spectrum, g is the acceleration of gravity, f_ς is the wave frequency, and f_P is the frequency of the wave energy peak. This function has dependence on wind speed at gravity wave frequencies where the peak of the spectrum is given by: $f_p = 1.56/U_{10}$ and $\hat{f} = {f_\varsigma}/{f_p} = \sqrt{{\kappa}/{\kappa_p}}$, where $\hat{f}$ is the nondimensional frequency and κ_p is the wave number at the peak of the wave spectrum [*Alves et al.*, 2003].

[32] We can relate S to F by changing variables from f_ς to κ yielding [*Janssen et al.*, 1998]:

$$F_\varsigma(\kappa) = S(f_\varsigma)\left(\frac{1}{\kappa}\right) 2\pi {d\omega_\varsigma}/{d\kappa}, \text{ where } \omega_\varsigma^2 = g\kappa + \gamma\kappa^3.$$

γ is the dynamic surface tension, equal to 7.0062×10^{-5} m^3/s^2 for pure seawater, but surfactants likely lower the value of γ, also decreasing the wave number of the peak of the curvature spectrum, $\kappa_m = (g/\gamma)^{1/2}$ [*Tsai and Liu*, 2003; *Munk*, 2009]. Using the above value for γ, we obtain:

$${d\omega_\varsigma}/{d\kappa} = \frac{g + 2.1 \times 10^{-4}\kappa^{-2}}{2\omega_\varsigma}, \text{ and the elevation spectrum:}$$

$$F_\varsigma(\kappa) = 0.03\kappa^{-4} \exp\left[-1.25\left({\kappa_p}/{\kappa}\right)^2\right]. \qquad (3)$$

[33] The elevation energy spectrum, $F_\varsigma(\kappa)$, is independent of the directionality of the wavefield, with units of m^4/radians^2. The wave model described by equation (3) is used as a starting point for the analyses below.

4. Acoustic Signal Generation

[34] To model the transfer of wave energy to the ocean floor using the Longuet-Higgins mechanism we follow *Farrell and Munk* [2008] using the equation developed by *Hughes* [1976] to predict the L-H pressure available at the ocean floor in terms of the wave elevation wave number spectrum and the overlap function:

$$F_P(\omega_P) = \frac{\pi}{8}\left(\frac{\rho}{c}\right)^2 \omega_P^6 \frac{\kappa F_\varsigma^2(\kappa)}{{d\omega_\varsigma}/{d\kappa}} I(\kappa),$$

$$\text{where } I(\kappa) = \int_{-\pi}^{\pi} H(\kappa,\theta) H(\kappa,\theta+\pi) d\theta. \qquad (4)$$

[35] F_P is the L-H pressure coming from the ocean surface above the hydrophone, ω_p is the angular acoustic frequency equal to $2\omega_\varsigma$, $\rho = 1025$ kg/m^3 is the standard seawater density, $c = 1500$ m/s is the speed of sound in the water, and $I(\kappa)$ is the overlap integral. In isotropic seas both $H(\kappa, \theta)$ and $I(\kappa)$ are equal to $1/(2\pi)$, or -8 dB.

4.1. Regional Seismic Contribution to the Signal

[36] F_P, the L-H pressure, is the observed signal if no seismic waves propagate to the hydrophone through the

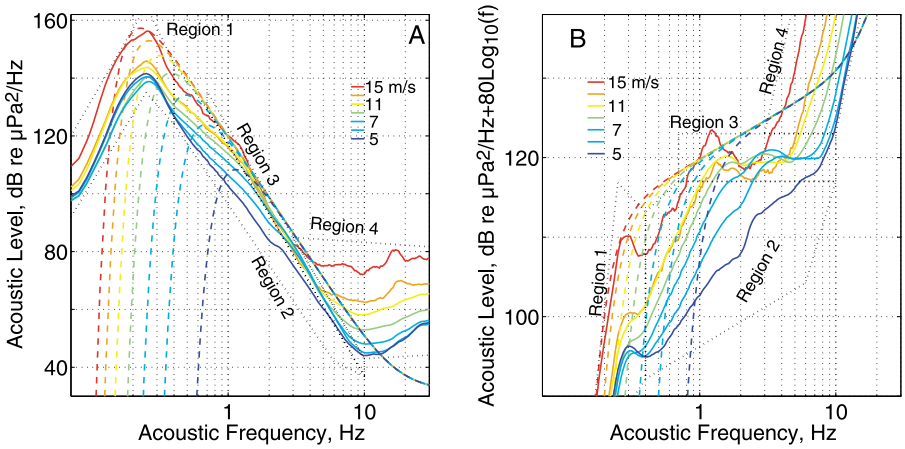

Figure 8. Initial L-H pressure model comparison to ACO data. The Pierson-Moskowitz wave elevation spectrum model (equation (3)) is transformed into acoustic level using equations (2)–(4) (dashed lines) for comparison with the ACO acoustic data (solid lines) that are smoothed by a 10-point boxcar filter for clarity in presentation. Colors indicate wind speeds from 5 to 15 m/s in 2 m/s steps. (a) Unrotated. (b) Rotated by f^8.

earth. At low frequencies, a fraction of this signal (F_s) will couple into seismic waves that propagate laterally through the earth where they can be observed by distant hydrophones and seismometers [*Longuet-Higgins*, 1950; *Hasselmann*, 1963; *Zhang et al.*, 2010]. If F_P and the seismic wavefield generated by the L-H mechanism are uniform in the region around the hydrophone, and if the transfer function from pressure-to-seismic waves is efficient enough, then the spatial integral of F_s, $F_m(R) \propto \int_0^R \int_{-\pi}^{\pi} F_s dr d\theta$, where r is the distance of the source from the hydrophone, added to F_p will constitute the signal observed at the hydrophone. The physical size of the region to be integrated depends on the seismic attenuation modeled by a constant Q. If the seismic waves are trapped near the ocean floor, and Q is infinite, there is no attenuation of the seismic waves, and conservation of energy requires that F_m increase linearly with radius of the region integrated (using the flat-earth approximation). Assuming a constant finite Q, attenuation will bound the integral, and the slope of the spectrum of F_m includes an additional $1/f$ term. The Q value governs the size of the region around the hydrophone that contributes to F_m. The higher the Q of the seismic waves, and the lower the frequency, the larger the region around the hydrophone that contributes to the observed energy [*Ardhuin et al.*, 2011]. At some high frequency F_m is negligible compared to F_P. At low enough frequencies, the F_m region will be large enough to include areas where the wind and other environmental characteristics, such as the influence of shorelines, are no longer uniform, and correlation with the local wind will decrease. Seismic stations on land will only detect the propagating portion of the energy, F_m, while hydrophones and ocean bottom seismometers will detect both F_m and F_p. *Chi et al.* [2010] and *Farrell and Munk* [2010] argue that high correlation between vertical seismic motion and pressure at an ocean bottom seismometer (OBS) implies that energy generated above the sensor (F_s) is dominating. *Chi et al.* [2010] observed high correlation at an OBS between vertical motion and pressure data above 0.2 Hz in 4726 m of water.

4.2. Acoustic Model Comparison to Data

[37] Figure 8 compares the F_p model provided by equations (2)–(4) to the ACO acoustic data for wind speeds from 3 to 15 m/s in 2 m/s steps assuming that the wavefield is isotropic, $I = 1/(2\pi)$, and that there is no contribution from propagation of seismic energy. Multiplying acoustic levels (rotating) by f^8 emphasizes the variations where the spectral slopes are steep (Figure 8b). While the model spectral levels are similar to the observations, there are large departures.

4.2.1. Discrepancies Between the Model and Data

[38] We identify discrepancies between the model and the acoustic observations in the four regions of the acoustic spectrum shown in Figures 7–9, 10b, and 14. In R1, Region 1(below 0.4 Hz), the wave model predicts strong correlation with wind speed, but very low correlation with wind speed is observed except above 11 m/s wind speed; in R2 where the slope of the acoustic spectra vary from f^{-4} to f^{-6}, the model predicts a larger increase in acoustic levels with increasing frequency than is observed; in R3 the slope of the saturated region is observed to be f^{-8} rather than the predicted slope of f^{-7} [*Farrell and Munk*, 2008], and the saturated region observed does not extend to the low frequencies predicted by the model; and in R4, the abrupt change in slope to f^{-2} is not predicted by the P-M model.

4.2.2. Modification of Model Spectral Slope in R3

[39] We first examine the discrepancy in slope in the saturated zone (R3). There are at least four possible sources of this discrepancy, inaccuracy in the slope of the model wave number spectrum above 0.5 Hz, variations in the overlap integral, effects of interactions with the ocean floor, and seismic contributions to the acoustic levels from regional sources. Few data are available concerning the slope of the wave elevation energy spectrum above 0.5 Hz where it may be complicated by Doppler shifting of short waves [*Longuet-Higgins*, 1950; *Donelan et al.*, 1997; *Munk*, 2009]. A change in slope of $F_\zeta(\kappa)$ from κ^{-4} to $\kappa^{-4.25}$ is enough to rectify the slope discrepancy, and *Hara and Belcher* [2002] suggest that sheltering of the short wavelength waves changes the slope of the equilibrium wave amplitude spectrum from κ^{-4}

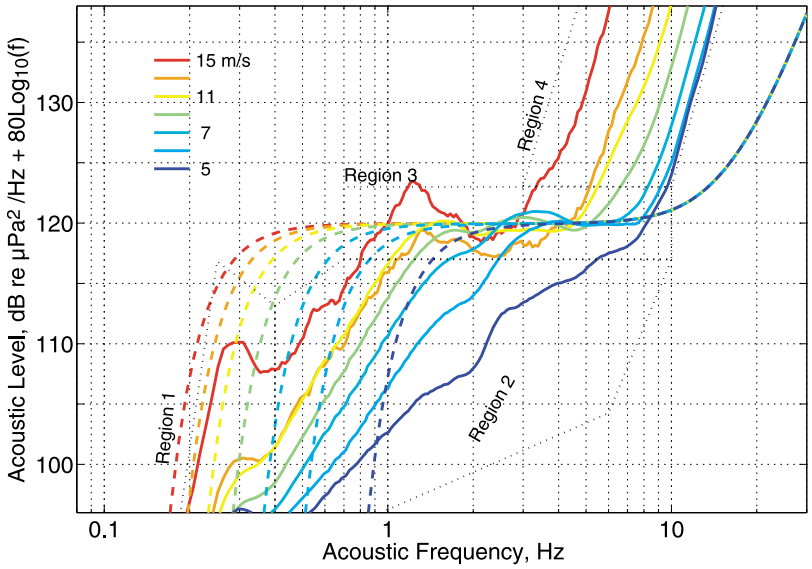

Figure 9. Comparison of the wave model transformed into acoustic levels using equation (5) (dashed) with the observed ACO acoustic levels (solid). The acoustic spectra have been smoothed by a 10-point boxcar filter for clarity in presentation.

to κ^{-5} above a particular wave number, κ_s, the sheltering wave number. They argue that κ_s decreases with increasing wind speed with values less than 100 for friction velocities greater than 0.6.

[40] If the slope discrepancy is caused by a variation in the overlap integral (I), then to correct the model acoustic spectrum slope in the saturated region requires that the overlap integral decrease as frequency increases, i.e., waves becoming more directional as frequency increases, the opposite of observations [*Hwang and Wang*, 2001; *Resio et al.*, 2011]. However, Doppler shifting would introduce apparent anisotropy. Interactions of the acoustic field with the ocean floor depend on the characteristics of the ocean floor and the height of the sensor above the ocean floor [*Kibblewhite and Wu*, 1996]. While it is possible that sediment interactions could modify the acoustic spectrum, resulting in a slope change of the acoustic spectrum from f^{-7} to f^{-8}, we have no reason to conclude that this is the case. It is also possible that the seismic contributions to the observed acoustic energy in the region (F_m) could provide the missing $1/f$ term. Since we have no reason to conclude that the discrepancy in slope results from any one of the above causes, we include a separate f_p^{-1} term in equation (5) to account for the discrepancy, noting that the origin of this term is undetermined, and that it may be valid only in the saturated region. The resulting pressure spectrum model is shown below:

$$F_p(\omega_p) = \frac{\pi}{8}\left(\frac{\rho}{c}\right)^2 \omega_p^6 \frac{\kappa F_\varsigma^2(\kappa)}{d\omega_\varsigma/d\kappa} I(\kappa)\, f_p^{-1}. \tag{5}$$

[41] Comparison of the model acoustic spectrum (equation (5)) and the data is shown in Figure 9. The 0.03 factor in equation (3) has been replaced by 0.12 to match the observed data level in the saturated region.

4.2.3. Inclusion of Ultra-gravities Into Model

[42] We now address the departure of the model spectrum defined by equation (5) from the data, where the slope of the observed spectrum changes from f^{-8} in R3 to a wind speed-dependent slope of f^{-2} in R4. The model displays no dependence on wind speed in this region, while the observed levels increase with wind speed. Substantial improvement in the agreement between the model and the data at high frequencies is obtained by including the ultra-gravity wave regime as in the works by *Banner et al.* [2000], *Liu and Yan* [1995], *Elfouhaily et al.* [1997], *Hwang and Wang* [2004], *Hwang* [2005], and *Farrell and Munk* [2008]. There are a number of important issues with measurements and modeling of the high wave number portion of the spectrum. One is that Doppler shifting of short (slow) waves makes transformation from apparent frequency into wave number particularly problematic [*Phillips*, 1985; *Hara et al.*, 1997]. Short waves "bound" to longer waves behave differently than free waves. Another complexity is that short waves are sheltered by the large, long waves [*Donelan et al.*, 1985; *Hara and Belcher*, 2002; *Hwang*, 2008]. Ultimately, the airflow over the waves and the resultant stresses have to be treated in a coupled wave boundary layer framework [*Donelan et al.*, 1997; *Hristov et al.*, 1998; *Kudryavtsev and Makin*, 2002; *Hara and Belcher*, 2002; *Mueller and Veron*, 2009].

[43] Rather than add the complexity inherent in the above models utilizing parameters that are not well constrained, we add a second empirical term to the wave model (equation (3)) that provides close agreement of the wave model with the acoustic spectrum, assuming that the directionality of the wavefield is isotropic, $I = 1/(2\pi)$.

$$F_\varsigma(\kappa) = 0.012\kappa^{-4}\exp\left[-1.25\left(\kappa_p/\kappa\right)^2\right] + 5.0\times10^{-6}\exp[7.2u^*]\kappa^{-1.58}\exp\left[-0.25((\kappa/\kappa_m)-1)^2\right]. \tag{6}$$

[44] The first term on the right in equation (6) is equation (3) (with 0.03 replaced by 0.012), and u^* is the

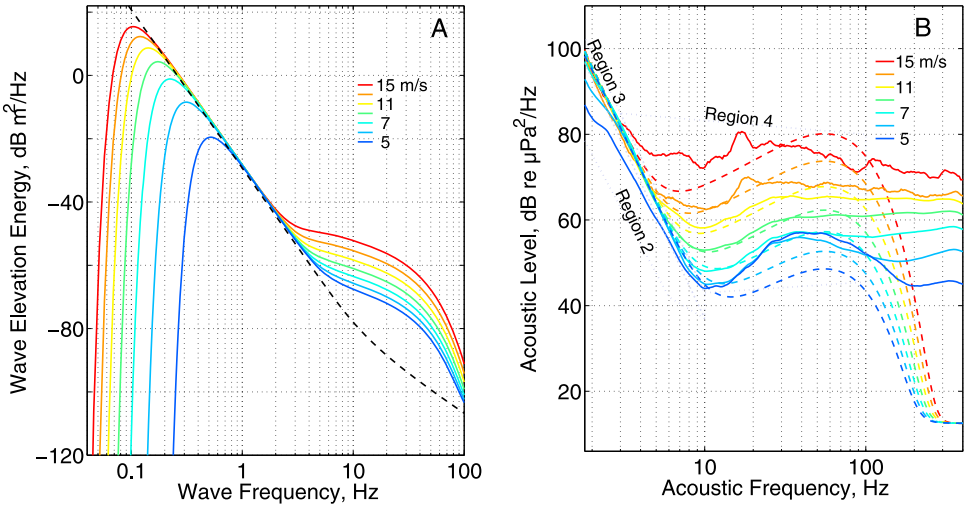

Figure 10. (a) Model wave elevation energy spectra. The dashed line shows the Phillips' saturation spectrum for reference. (b) Modified acoustic spectrum model (dashed) and data rotated by f^8. The observed acoustic spectra (solid) have been smoothed by a 10-point boxcar filter for clarity in presentation.

friction velocity [*Elfouhaily et al.*, 1997]. The 2nd term dominates in R4. The 2nd exponential of the 2nd term is from *Xiradakis* [2009] with κ_m = 280 (the wave number of the peak of the wave curvature spectrum), to provide a reasonable visual fit to the acoustic data at frequencies up to about 80 Hz. If a higher value for κ_m is used, such as κ_m = 363, the wave number of the capillary peak for pure seawater [*Elfouhaily et al.*, 1997], the model acoustic levels are higher than observed at high frequencies implying that the wavefield is becoming either more directional with increasing frequency, which is unlikely, or that surfactants are decreasing the surface tension and the peak of the curvature wave spectrum [*Hara and Belcher*, 2002].

[45] The resulting wave elevation model is shown in Figure 10a, and acoustic spectral data and the model obtained by substituting $F_\zeta(\kappa)$ from equation (6) in equation (5) are shown in Figure 10b. For wind speeds from 7 to 11 m/s, the wave model transformed into L-H pressure fits the acoustic data well at acoustic frequencies in R3 and up to about 80 Hz in R4. A power law function of u^*, rather than the exponential function of u^* used in equation (6), was found to model the data equally well for U_{10} between 7 and 11 m/s. Data at higher wind speeds are required to resolve the issue of which is the appropriate model. At lower wind speeds and higher frequencies the observed acoustic levels are higher than predicted by the model and are either controlled by factors other than wind speed, they reflect changes in the physics underlying the wave spectrum, or they result from incompleteness in the energy transfer functions. Above about 80 Hz it seems likely that the acoustic background is generated by sources other than the L-H mechanism, although the frequency where the transition to acoustic sources occurs is not clear.

4.2.4. Wavefield Directionality

[46] We now investigate wave directionality to find a model that maximizes the consistency between wave observations and the observed acoustic data in R2, where the wave spectrum model is saturated but the acoustic levels increase with wind speed. The spreading function, $H(\theta)$, and resulting overlap integral, I, (equation (4)), are critical in determining the amount of energy transformed into deep-ocean acoustic energy by the L-H mechanism. Processes that shape the directional wave spectrum are discussed by *Donelan et al.* [1985], *Banner* [1990], and more recently by *Resio et al.* [2011]. In the absence of swell, the spreading function is expected to be symmetric about the wind direction and dependent on frequency, fetch, wind speed, and wave age [*Donelan et al.*, 1985]. Near the peak of the wave spectrum, energy is concentrated close to the direction of the wind stress vector [*Mitsuyasu et al.*, 1975; *Munk*, 2009]. For wave numbers/frequencies above the peak, the directional spectrum widens and appears to become bimodal. The directional spectrum and overlap integral for large wave numbers is still very much an issue [*Farrell and Munk*, 2008; *Munk*, 2009], although the existence of a bimodal distribution with the angular separation increasing with wave number has now been established [*Forristall and Ewans*, 1998; *Wang and Hwang*, 2001; *Hwang and Wang*, 2001; *Toffoli et al.*, 2010]. *Resio et al.* [2011] suggest that the directional distribution widens to near-isotropic conditions above approximately 8 times the peak wave frequency as a result of momentum conservation considerations.

[47] The importance of the directionality of the wavefield is seen in Figure 11, showing $H(\theta)$, the normalized wave amplitude, versus angle from the downwind direction for 0.2, 0.4 and 0.8 Hz waves for a wind speed of 10 m/s, based on the *Mitsuyasu et al.* [1975] model as shown by *Hwang and Wang* [2001], and for a bimodal model [*Ewans*, 1998] at a nondimensional frequency of 10. For highly directional waves, as shown by the 0.2 Hz curve in Figure 11, the overlap integral (I) is very small, yielding little acoustic signal at the deep-ocean floor (equation (5)). For nearly isotropic wavefields, as shown by the 0.8 Hz curve in Figure 11, the overlap integral approaches $1/(2\pi)$, or −8 dB. Although higher overlap integral values are possible when the seas are dominated by opposing wavefields, the overlap integral is not likely to be appreciably larger than $1/(2\pi)$ for wind-driven seas [*Farrell and Munk*, 2010]. For the case of

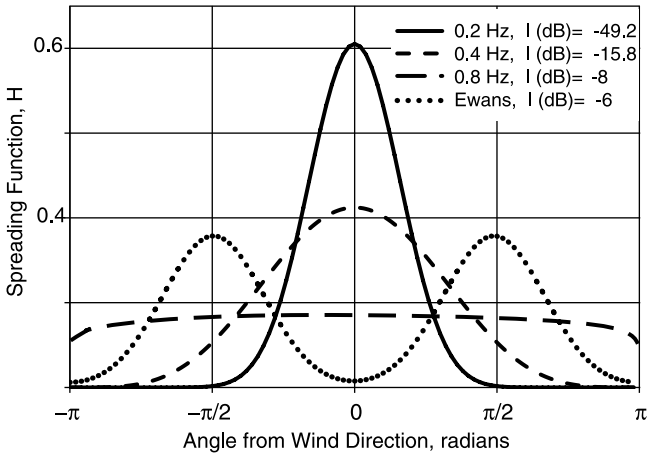

Figure 11. The spreading function, H(θ), is shown for several models of directionality using the *Mitsuyasu et al.* [1975] model for a 10 m/s wind speed at different frequencies and the *Ewans* [1998] bimodal spreading model for nondimensional frequency of 10.

bimodal seas [*Ewans*, 1998], the overlap integral is found to rise to values of less than 0.5 (−6 dB) near $\hat{f} = 10$ and then decrease to approximately $1/(2\pi)$ at higher frequencies.

4.2.5. Model Overlap Integral

[48] The acoustic model developed up to this point assumes that the wavefield is isotropic, and thus the overlap integral has a constant value of −8 dB. If we assume that the observed acoustic signal consists of only F_p with no contribution from F_m, then equation (6) can be solved for I as a function of the observed acoustic spectrum divided by a function of the model wave spectrum:

$$I(\kappa) = \frac{F_P(\omega_P)}{\frac{\pi}{8}\left(\frac{\rho}{c}\right)^2 \omega_P^5 \frac{\kappa F_\varsigma^2(\kappa)}{d\omega_\varsigma / d\kappa}}. \quad (7)$$

[49] The estimated overlap integral obtained from the acoustic data and the wave model using equation (7) is plotted against wind speed and frequency in Figure 12. Blue areas are where I-values are lower than about −12 dB, implying either 1) a strongly directional wavefield, 2) higher than expected wave energy, or 3) lower than expected acoustic levels. Low values of I on the high-frequency side of the wave energy peak (shown as white circles in Figure 12) indicate strong directionality of waves near the energy peak, since the wave model and the acoustic spectrum are well constrained at these frequencies. If an appreciable fraction of the observed energy is F_m, then the estimated I-values are higher than the actual values, thus the wavefield is more directional than indicated in Figure 12 at low frequencies, and, assuming that F_m values decrease with increasing frequency, the slope of the observed acoustic spectrum could be steepened by contributions from F_m, possibly explaining the slope discrepancy in R3 discussed in section 4.2.2.

[50] Below the wave energy peak, the I-values are very high (red) indicating that either 1) the wavefield is strongly dominated by a pair of opposing waves, 2) the wave energy is much less than predicted by the wave model, or 3) the observed acoustic levels are higher than predicted. Only the third option is likely since wave energy at frequencies near the wave energy peak is well known, thus the acoustic energy observed below the wave energy peak is higher than expected and not generated by local seas. Similarly, sources of energy that are not related to the local wind field appear to dominate the spectrum above 6 Hz at wind speeds below 4 m/s. The I-values in Figure 12 become increasingly positive above about 50 Hz, implying either that 1) the wavefield is becoming dominated by a set of opposing waves, 2) the predicted wave energy is too low, or 3) that the acoustic energy observed is higher than expected from the model. These high I-values are likely the result of acoustic sources other than F_p dominating the spectrum at low wind speeds, while at frequencies above 70–80 Hz poor knowledge of the wave spectrum could also be important.

[51] Reasonable agreement with the acoustic data is obtained if the overlap integral rises from small values at low

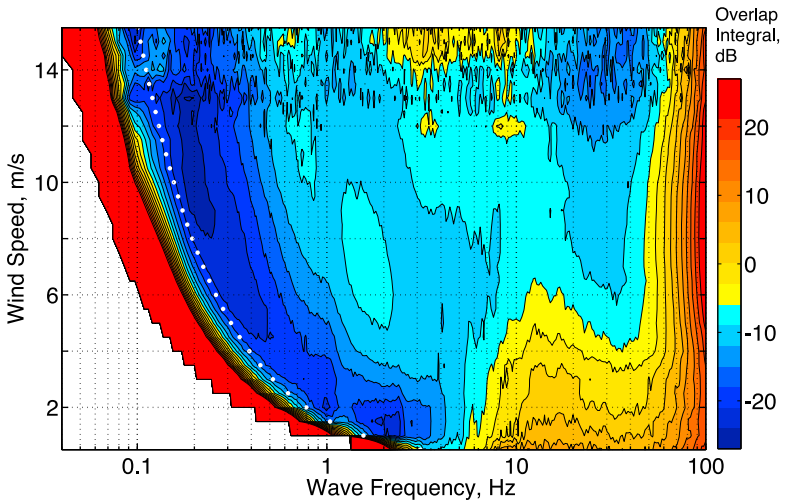

Figure 12. Overlap integral value estimated from model wave spectra and ACO acoustic observations showing the dependence on wind speed and frequency. White circles show the theoretical peak of the wave energy spectrum at each wind speed.

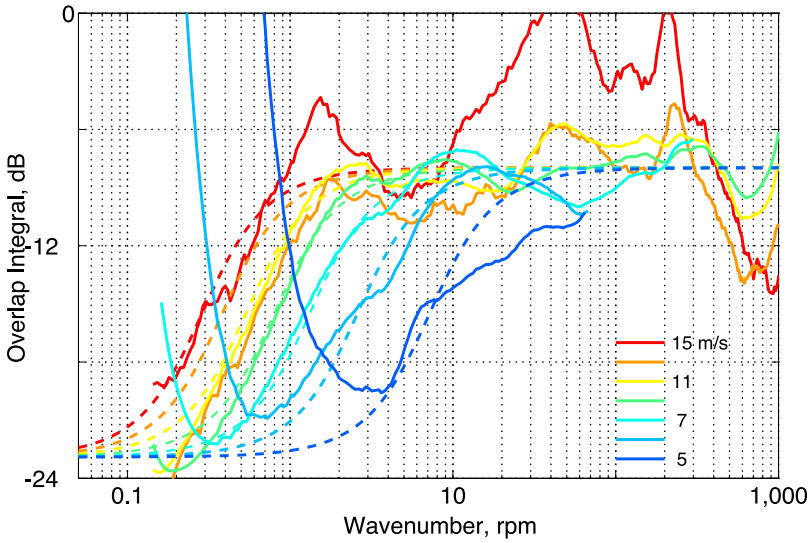

Figure 13. Comparison of the equation (8) model overlap integral (dashed) to the overlap integral estimated from the acoustic data and wave model (solid). The acoustic spectra have been smoothed by a 10-point boxcar filter, and spectral values that are in the noise and/or controlled by factors other than wind have been removed for clarity. Colors represent different wind speeds from 5 to 15 m/s.

frequencies to values near $1/(2\pi)$ above about 1 Hz, consistent with directional spectral models [*Mitsuyasu et al.*, 1975; *Ewans*, 1998; *Wang and Hwang*, 2001; *Hwang and Wang*, 2001; *Toffoli et al.*, 2010; *Resio et al.*, 2011] that imply asymptotic approach to isotropic conditions at higher frequencies. Again, assuming that the observed acoustic spectrum reflects only F_p and $F(\kappa)$ (equation (6)), we obtain an empirical function (equation (8)) for I shown by the dashed lines in Figure 13 that is consistent with the estimated I obtained from equation (7) (solid lines) [*Alves et al.*, 2003].

$$I_{dB}(\kappa) = 9.5\tan^{-1}\left[0.04\left(\kappa/\kappa_p\right)^{1.7}\right] - 22.9 \qquad (8)$$

$$\text{where } \kappa_p = \frac{4\pi^2}{g}\left(f_p\right)^2 = \frac{4\pi^2}{g}\left(\frac{1.56}{U_{10}}\right)^2 = \frac{9.8}{U_{10}^2}.$$

[52] The constants in equation (8) have been adjusted by eye to fit the ACO pressure data in the 0.4 to 2 Hz range. The model values of I are within 2 dB of the estimated overlap integral based on the data from $0.5 < \kappa < 300$ rpm and $4.5 < U_{10} < 11$ m/s. The function shown is similar to those presented by *Mitsuyasu et al.* [1975] and *Cato* [1991] except that the minimum value of I is limited in equation (8) to model the effects of gustiness and other variations in wind direction within the fetch. The spreading function is extended to frequencies above R3, although we cannot separate the spreading function from other characteristics of the wave spectrum beyond R3; readers should not assume that the data warrant the conclusion that isotropic conditions or that the $1/f$ term appended to equation (5) are appropriate above 10 Hz. Also, if F_m is dominant, the actual values of I at low frequencies are likely to be lower than calculated for F_p only.

4.3. Final Acoustic Model

[53] The final acoustic spectral model, based more on the observations than on the physics involved, is compared to the ACO acoustic data in Figure 14. While there are notable discrepancies between the model and observations, the model provides a starting point for discussion. The model generally agrees with the acoustic data within 2 dB from 0.5 Hz to 80 Hz for wind speeds from 7 to 11 m/s. There are not enough data at higher wind speeds to provide a good comparison to the model. We include the data at 13 and 15 m/s wind speed for completeness, but, as these spectra represent only a few hours of data, they do not have the statistical robustness present at lower wind speeds. Observed acoustic levels are higher than model values for wind speeds <2.5 m/s over most of the spectrum, and are likely influenced by variables other than wind speed at ALOHA. The model and data diverge at frequencies near and below the wave energy peak and at acoustic frequencies above ~80 Hz. This model does not take into account likely seismic propagation of remote L-H pressure signals to the hydrophone discussed below.

4.4. Origin of Low Frequency Acoustic Background

[54] To investigate the source of energy in R1, the low frequency band near and below the wave energy peak where acoustic energy does not correlate with local wind speeds (Figure 4), we compare the ACO energy spectral levels with observed ocean wave and seismic energy obtained at the locations indicated in Figure 1. If the double-frequency L-H mechanism is the dominant energy pathway for local wave energy to be observed at ACO, correlation of the acoustic spectral time series with the wave spectral time series is expected to be high where the acoustic frequency is twice the wave frequency. To verify this we correlate the ACO acoustic spectral time series with wave spectral time series from the Waimea Bay buoy. Although this buoy is sheltered from swell from the south and east, and is 115 km distant from the ACO, much of the wave activity present at Station ALOHA should be observed at the buoy, though with some leads and lags depending on frequency and wave direction.

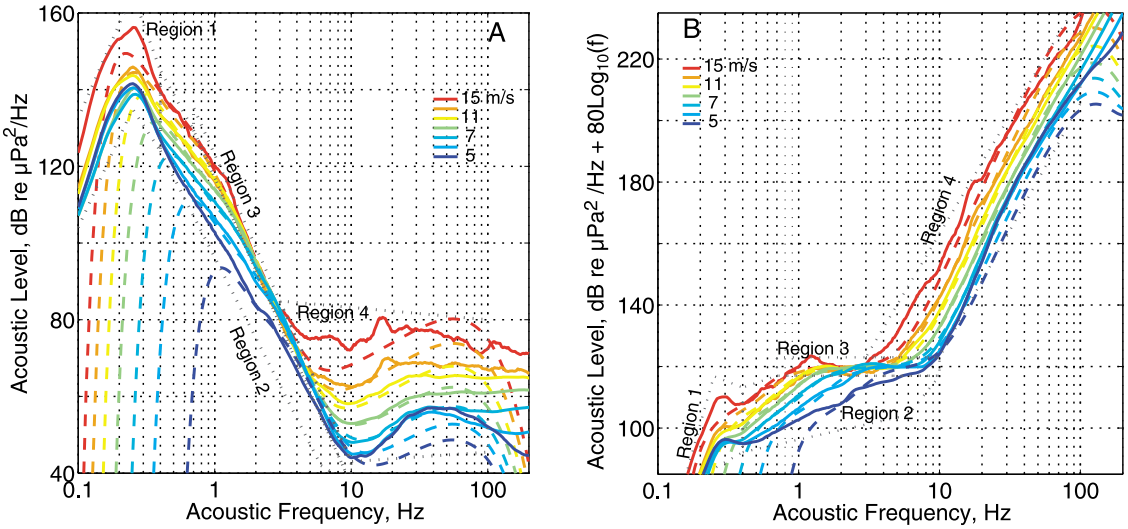

Figure 14. Unrotated and rotated comparison of the resulting model of the ACO acoustic data (dashed lines) compared to the observed spectra (solid). Compare these plots with those in Figures 8–10.

4.4.1. Coherence of Acoustic and Wave Spectra

[55] The two-dimensional coherence plot correlating the Waimea Bay wave spectral time series with the ACO acoustic spectral time series is shown in Figure 15a. Unlike the acoustic spectra used above, the spectral time series used to generate Figures 15, 16, and 18 contains all available data at each frequency, not selected for particular characteristics. The coherence shown is the maximum observed for lags up to ±20 h (see Figure 4). For discussion purposes it is convenient to divide Figure 15a into the four quadrants bounded by lines at 0.12 Hz wave frequency and 0.4 Hz acoustic frequency. The 0.12 Hz boundary is near the peak of the trade wind swell at 8-s period, and 0.4 Hz is the frequency below which coherence of the acoustic signal with local winds decreases rapidly (Figure 4). Wave and acoustic energy display high correlation in the lower left ("LL") and upper right ("UR") quadrants, and poor correlation in the other two quadrants. We discuss the LL quadrant first and then explore the possible explanations for the high correlations in the UR quadrant.

[56] The maximum correlation between waves and the acoustic levels in the LL quadrant of Figure 15a occurs when the acoustic frequency is twice the wave frequency, strongly supporting the hypothesis that local ocean waves contribute to the observed acoustic energy, and that the L-H mechanism provides the dominant pathway for this energy. However, the lack of correlation of acoustic energy with wind speed below 0.4 Hz (Figure 4) implies that this energy was not generated by local wind seas. One possible source for this acoustic energy is swell from distant storms [*Chevrot et al.*, 2007; *Ardhuin et al.*, 2011], but such swell is highly directional and narrow band, and the requirement for a set of opposing swell near Hawaii uncorrelated to the local wind speed is likely not common.

[57] Another possibility is that the opposing energy is supplied by reflected swell near coastlines [*Elgar et al.*,

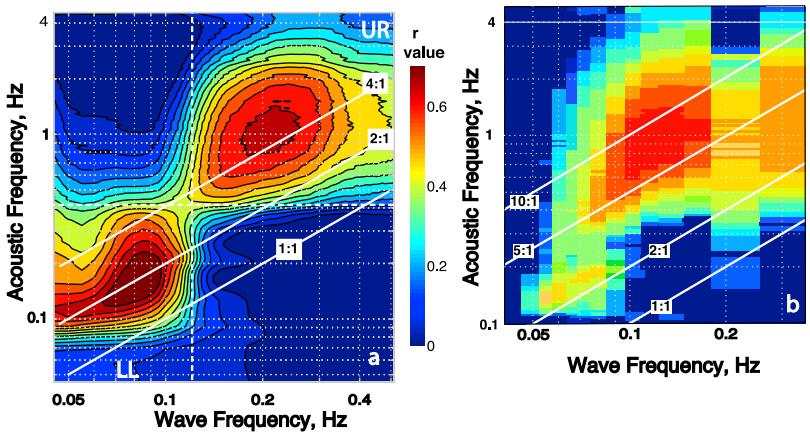

Figure 15. Wave/acoustic coherence: (a) ACO and (b) Wake Island. The solid white lines indicate constant ratios of acoustic frequency to wave frequency. The dashed white lines in Figure 15a divide the plot into four quadrants discussed in the text. Figure 15b displays similar data obtained from a hydrophone in deep water near Wake Island (modified from *McCreery* [1992]).

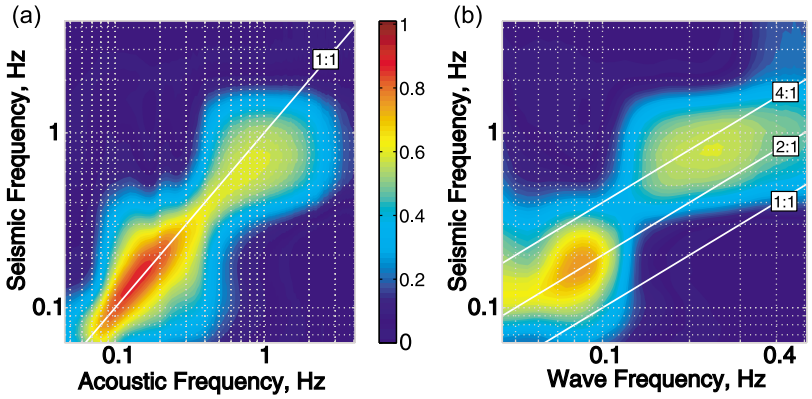

Figure 16. (a) Acoustic (ACO) signal coherence with vertical seismic (KIP) spectral time series from Oahu. The signals correlate with a 1:1 frequency ratio. (b) Waimea wave spectral time series coherence with the KIP seismic spectral time series.

1994; *Bromirski et al.*, 1999, 2005; *Chi et al.*, 2010]. Double-frequency seismo-acoustic signal generated by wave interactions near coastal waters will have energy proportional to the product of the amplitude of the incident and reflected waves [*Longuet-Higgins*, 1950]. The amplitude of the reflected waves, and thus the acoustic signal, will depend on wave direction, amplitude, and frequency, shoreline geometry, and reflection coefficients, making quantification difficult. Ocean wave reflection coefficients are expected to be larger for low frequency waves because of increased scattering and dissipation of high frequencies by bottom roughness, further enhancing the double-frequency correlation of wave and acoustic spectra in the LL quadrant of Figure 15a relative to the lower right quadrant. Steep shorelines, such as the cliffs on the north coast of Molokai, are likely strongly reflecting.

4.4.2. Coherence of Acoustic and Seismic Spectra

[58] If the energy in the LL quadrant of Figure 15a originates from reflection from shorelines, as proposed by *Bromirski et al.* [1999, 2005], or by generation of the seismic energy in the deep ocean under storms [*Cessaro*, 1994; *Kedar et al.*, 2008; *Zhang et al.*, 2010; *Chi et al.*, 2010; *Ardhuin et al.*, 2011], radiating away from the source region at seismic speeds (~1.5–8 km/s), it should be detected almost simultaneously by seismic stations and nearby ocean acoustic sensors. The two-dimensional coherence between the vertical seismic spectral time series recorded at the KIP seismic station on Oahu (see Figure 2) with the acoustic signals at ACO is shown in Figure 16a. The correlation is maximum at a 1:1 frequency ratio with the strongest correlation below 0.4 Hz, and the lag at maximum correlation is zero (within the hourly resolution of the data). This observation implies that the hydrophone and seismic signals in the LL quadrant have contributions from the same source, and, referring to Figures 15a and 16b, that source is strongly related to the ocean wavefield near Hawaii. The two-dimensional seismic to ocean wave coherence (Figure 16b) is similar to the ACO-ocean wave correlation (Figure 15a) with quadrant boundaries at the same frequencies. The correlation of the wave spectra with the seismic and acoustic spectra implies that the local wavefield is responsible for a major fraction of the observed background. The low 2:1 correlation in the lower right quadrants of Figures 15a and 16b implies that L-H energy generated by either shoreline reflection or by deep-ocean generation near Hawaii is limited to wave frequencies below 0.15 Hz.

[59] A similar observation to that shown in Figure 15a, was described by *McCreery* [1992], who used acoustic spectral data from the Wake Island deep-ocean hydrophone array and SOWM wave energy estimates [*Pierson*, 1982] to generate the coherence plot shown in Figure 15b. The 2:1 correlation peak in the LL quadrant of Figure 15b is offset to the left from the 2:1 frequency ratio, possibly a result of inaccuracies in the SOWM wave model. The Wake Island correlation shows two important differences from the ACO coherence plot (Figure 15a). The 2:1 correlation peak at Wake is much less pronounced than it is at ACO, and the high correlations in the UR quadrant extend into the lower acoustic frequencies in the upper left quadrant. These observations are qualitatively explained by the greater distance from the Wake Island hydrophone to extensive coastlines. ACO, being close to the Hawaiian Islands, may record more energy derived from wave interactions in the island coastal waters, increasing the 2:1 correlation peak, whereas the Wake hydrophone array is far from long coastlines and observes less of the 2:1 seismic energy that correlates with the local wavefield.

[60] Based on these observations, it appears that a large fraction of the acoustic energy observed at ACO below 0.3 Hz is not generated directly by local wind-generated seas, but instead propagates to the hydrophone as seismic waves generated nearshore by the interaction of incident and reflecting waves. While some of this wave-wave interaction energy is likely generated in the deep ocean when swell directions are opposing [*Kedar et al.*, 2008; *Ardhuin et al.*, 2011], it appears that signal generated by interactions of incident and reflected waves in coastal waters is also important [*Bromirski et al.*, 2005; *Traer et al.*, 2008; *Chi et al.*, 2010].

[61] *Webb and Schultz* [1992] showed that the amount of energy in the microseism peak near 0.2 Hz correlates with the size of the ocean basin, with the energy levels in the Pacific basin about 20 dB higher than the Atlantic and 40 dB higher than under the arctic ice. The levels in the Atlantic

and Pacific are nearly the same above ~1 Hz, but are 30 dB lower in the Arctic at 1 Hz. Although the microseism signal is known to propagate across continents [*Bromirski*, 2001], seismic attenuation is apparently strong enough that regional and local contributions to the microseism energy dominate the spectrum when a wavefield is present, such as under the North Pacific trade winds.

4.5. Higher Frequency Wave-Acoustic Coherence

[62] A transition from the 2:1 correlation peak observed in the LL quadrant to a strong, broad coherence peak above 0.4 Hz acoustic frequency in the UR quadrant is observed in Figures 15a and 15b, and also in Figure 16b. A sharp correlation peak or line, such as that in the lower left quadrant of Figure 15b, implies that the spectra at the two frequencies involved correlate with each other but adjacent frequencies in the same data set do not. On the other hand, broad correlation peaks imply that the spectral time series are correlated over a range of frequencies.

[63] The acoustic and seismic frequencies at maximum correlation are about 4–6 times the wave frequency rather than twice the frequency observed in the UR quadrant; i.e., 0.2 Hz ocean waves correlate best with 1 Hz acoustic levels and poorly with acoustic signals at 0.4 Hz. One Hz L-H acoustic energy will correlate with 0.2 Hz wave energy only if the 0.2 Hz wave energy correlate with the wave energy variations at 0.5 Hz, indeed, the *r*-value between the 0.5 Hz wave spectral time series and the 0.2 Hz wave spectrum time series is 0.57. Thus, the broad 5:1 acoustic frequency-to-wave frequency correlation peak in the UR quadrant is likely due to a combination of the lack of opposing wave energy from 0.12 to 0.5 Hz resulting in low L-H energy, and a strong correlation between the wind-sea wave spectral time series and wind speed over a broad range of frequencies.

5. Discussion

[64] While the results above are constrained by the characteristics of the ocean floor pressure background levels and correlations to nearby wind, wave, and seismic data, nonlinear relationships and the number of variables and parameters that can influence the results make it difficult to separate and quantify the diverse mechanisms that are responsible for the observed background levels. Possible driving mechanisms and characteristics of the environment that shape the acoustic spectrum are discussed below.

5.1. Background Levels Below 0.4 Hz

[65] The acoustic background levels at frequencies below 0.4 Hz do not correlate well with the local wind speed, but they do correlate well with the regional wave spectra and seismic background levels. The implication of these observations is that the acoustic background below 0.4 Hz is not generated at ACO, but is generated by wave interactions through the L-H mechanism at some distance from the hydrophone with the energy subsequently transmitted through the earth as seismic waves. This possibility was considered by *Longuet-Higgins* [1950], and more recently by *Kedar et al.* [2008] and *Ardhuin et al.* [2011]. In their analyses, wind and wave hindcast models were analyzed to estimate wave directional spectra over an area, which was then integrated to determine the energy observed at particular seismic stations. Reflections from shorelines were not included in the *Kedar et al.* [2008] model, but they are parameterized in the *Ardhuin et al.* [2011] model.

[66] *Ardhuin et al.* [2011] concluded that seismic energy due to wave energy reflected from the Hawaiian coastlines was insignificant compared to seismic energy produced regionally by the L-H mechanism in deep water. However, their model does not predict the correlation boundary near 0.4 Hz below which the acoustic background no longer correlates with the local wind speed. Such a boundary might be generated by the island coasts that act as fixed sources of L-H pressure generated by the interaction of incident and reflected swell [*Zhang et al.*, 2010]. If this hypothesis is correct, energy from reflections of swell from the islands could be a dominant source of microseism energy below 0.3 Hz, just below the boundary between R1 and R2. If the hydrophone were farther from the coasts, a lower bounding frequency between R1 and R2 could be expected.

[67] Storms generate long-period swell that can propagate across the Pacific Ocean, and such swell from remote storms can oppose Hawaii regional swell energy [*Ardhuin et al.*, 2011]. This is rare, however, given the climatological winter storm tracks and trade wind patterns of the subtropics. Storm centers, where opposing wave energy at frequencies <0.1 Hz is most probable, rarely pass within 1000 km of the main Hawaiian Islands. Since common trade wind seas have periods shorter than 8 s, local seas will rarely contribute to L-H acoustic energy at frequencies below 0.25 Hz. Waves with periods shorter than 20 s generated 1000 km from the islands would take more than 18 h to arrive at Hawaii, and would likely not meet opposing waves near the islands, unless reflected near Hawaiian coastlines. Since common trade wind seas have periods shorter than 8 s, local seas will rarely contribute to L-H acoustic energy at frequencies below 0.25 Hz.

[68] Since the land seismometers can have no contribution from waves above it, unlike the hydrophone, the wave-correlated seismic energy observed at KIP must be some combination of deep-ocean and reflected L-H energy. Seismic energy from the impact of breaking waves at the shoreline might be responsible for the correlation at a 1:1 frequency ratio near 10-s period in Figure 15a that is not seen in Figure 15b where nearby coastlines are absent. The correlations shown in Figures 15a and 16a strongly imply that a local deep-ocean L-H contribution to the seismic spectrum is present up to almost 3 Hz, but that energy from opposing waves is absent from 0.15 Hz up to about 0.4 Hz wave frequency, where little correlation is observed at a 2:1 frequency ratio. For comparison, since no long steep coastlines are present near the Wake Island hydrophones, and both Wake and the Hawaiian Islands have similar trade wind climates, the paucity of correlation in the LL quadrant of Figure 15b compared with Figure 15a implies that much of the energy observed below 0.3 Hz at ACO is generated from waves reflected from Hawaiian coasts, while that at Wake is generated near distant shorelines and by deep-ocean storms.

5.2. High Frequency Isotropy

[69] We deduce that the overlap integral approaches a constant value at the high end of the ocean wave equilibrium

region implying near-isotropic conditions. What are the mechanisms that create a more isotropic directional spectrum at higher frequencies? In addition to wave-wave nonlinear interactions that lead to increased energy in cross-wind wave numbers as discussed earlier, we expect that the upwind energy in the cross-wind wave numbers will increase with stronger wind speeds because of other nonlinear energy transfers including micro- and macro-breaking [*Resio et al.*, 2011].

[70] Theoretical, observational and numerical investigations of surface waves have led to the conclusion that energy from the wind field is most strongly coupled into the short ("ultra-gravity") wave portion of the spectrum (above 1 Hz wave frequency) [*Munk*, 2009] where it is transferred to longer scales by weak nonlinear wave-wave interactions lost directly to turbulent dissipation by wave breaking [*Hasselmann et al.*, 1976]. Maximum breaking probability occurs between $\hat{f} = 1$ and 1.6, depending on peak wave steepness [*Banner et al.*, 2000], rather than at the peak. Some energy from the wind input is also transferred to shorter wave numbers as parasitic capillary waves through micro-breaking, with subsequent dissipation [*Kudryavtsev et al.*, 1999]. However, this latter wind energy sink is small compared to the energy radiated away and eventually dissipated by long gravity waves. Another problem is that most wave models assume that all of the energy involved in wave breaking is dissipated immediately [e.g., *Banner and Peregrine*, 1993; *Melville*, 1996], but this is unrealistic.

[71] For stronger winds, ultra-gravity waves are generated directly by breaking wave jet penetration and splashing, and some energy is radiated from the subsequent turbulent region as ultra-gravity waves [*Yarin*, 2006]. The latter mechanism for generating ultra-gravity waves through breaking depends on the intensity of the turbulence, which depends on the nature of the breaking event (spilling versus plunging). Clearly, plunging breakers are more energetic, and they also generate more waves by splashing. The short waves generated by spilling and plunging breakers are nearly isotropic [*Kudryavtsev and Johannessen*, 2004], consistent with observations by *Banner et al.* [1989], and supported also by laboratory experimentation [*Rozenberg and Ritter*, 2005]. Thus, ultra-gravity waves should contribute disproportionately to the overlap integral and the acoustic pressure spectrum at the seafloor. The generation of short waves by wave breaking depends on the frequency and intensity of breaking events, which increase in proportion to u_*^3 [*Melville and Matusov*, 2002].

[72] Another issue is that standard wave models parameterize the momentum flux from the wind to the wavefield as a function of the mean wind, ignoring the details of atmospheric turbulence. At lower wind speeds, we expect that the unsteadiness of the wind contributes to crosswind wave number components [*Hwang and Wang*, 2001]. *Carswell et al.* [1999] used airborne microwave radar measurements to show that the cross-wind component of the short surface wavefield is affected by turbulent fluctuations of the wind. The standard deviation of the wind speed was found to be about 5% of the hourly averaged mean wind speed in the range of 1–10 m/s. Of more interest here is the finding that the standard deviation of the wind direction increases as the mean wind speed decreases. The wind direction deviation was always more than 10° in the 1–10 m/s range, reaching about 30° or greater for 1 m/s winds.

[73] Wave directionality at Bragg scattering wavelengths (0.04–0.1 m, or κ = 65–170 rpm) inferred from microwave scatterometers [*Janssen et al.*, 1998] does not contradict the approach to isotropic conditions discussed above. *Hwang* [1997] discusses nonlinearities that may contribute to anisotropic Bragg scattering. Also, the overlap integral is within a few dB of −8 dB with moderate anisotropy, within the uncertainty of our estimates.

5.3. Correlation of Acoustic Levels With the Wave Peak: Nondimensional Frequency

[74] We expect that the directional spectrum approaches near-isotropic conditions because of the secondary generation of short waves through breaking as discussed above. Of interest is the degree to which the omnidirectional spectrum and the directional spectrum scale with the wave peak frequency, or whether additional wind factors have to be accommodated to model our observations. To display the relationship of observed spectral levels to the peak of the wave energy spectrum it is insightful to use nondimensional frequency, $\hat{f}$, rather than frequency as the independent variable. When plotted against nondimensional frequency, wave spectra tend to have similar shape, independent of wind speed [e.g., *Donelan et al.*, 1985]. Similarly, plotting the acoustic levels rotated by f^8 (Figure 14b), and the overlap integral (Figure 13) against nondimensional frequency, shown in Figures 17a and 17b respectively, implies the acoustic levels and overlap integral values are clearly related to the frequency of the wave energy peak. Both collapse into curves that show little dependence on wind speed when plotted against nondimensional frequency, except at low wind speeds in R4 where other acoustic sources likely mask the L-H pressure signal.

5.4. Transition to Equilibrium Conditions

[75] *Hwang and Wang* [2001] suggest that the transition between the wave equilibrium range and the saturation range occurs at $\kappa/\kappa_p = 6.5 \pm 2$, or $\hat{f} = 2.1$–2.9. The results shown in Figure 17 show a change in spectral slope occurring near $\hat{f} = 5$, in the transition from low overlap integral values to a constant overlap integral, but this should not be confused with the transition to saturation of the wave spectrum. The omnidirectional wave spectrum does not depend on directionality, while the acoustic spectrum is strongly dependent on the directionality of the wavefield.

[76] Based on Figure 17a, transition from saturation (R3) to ultra-gravity waves (R4) is observed near $\hat{f} = 20$ (κ/κ_p = 400), at least for wind speeds above 4 m/s. The wave number of this transition was termed the join wave number, κ_{join}, by *Janssen et al.* [1998], and its value is likely rooted in the physics of wave generation [*Kudryavtsev and Makin*, 2002].

[77] Examples of spectrograms from August 2007 show the dependence of both gravity and ultra-gravity wave energies on $\hat{f}$ (Figure 18). Rotated acoustic levels above 123 dB are in R4, levels between 117 and 123 dB are in R3, and levels below 117 dB are in R2 (see Figure 7). The prevalence of horizontal contours up to $\hat{f} > 300$ in Figure 18c supports the hypothesis that the acoustic levels are strongly dependent

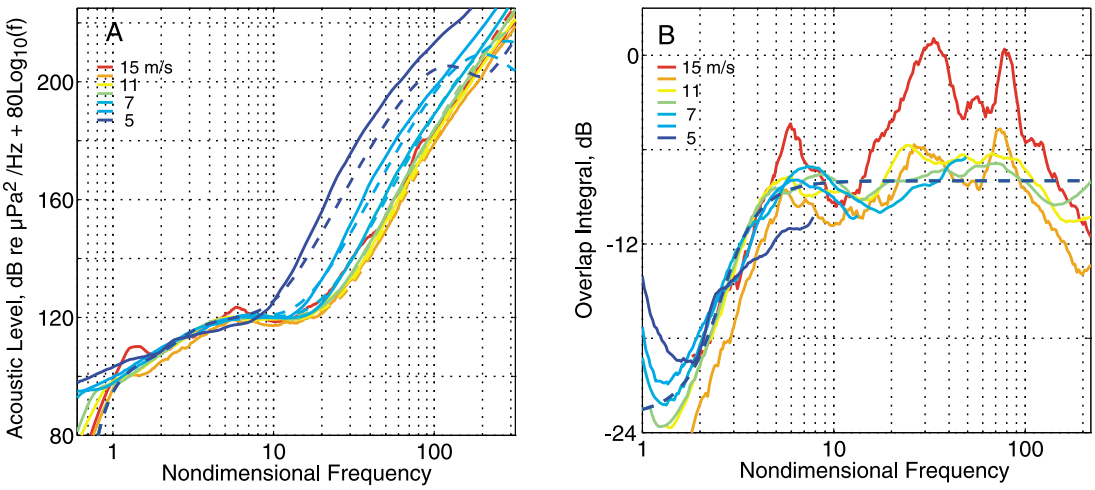

Figure 17. (a) Acoustic spectra rotated by f^8 (solid) and acoustic model (dashed) plotted against nondimensional frequency ($\hat{f} = f/f_p$). (b) Calculated overlap integral (solid) and model overlap integral (dashed) plotted against nondimensional frequency.

on the wave energy peak frequency up to frequencies of ~80 Hz. The only model dependence of this plot is the frequency of the wave peak. At times of low wind speed, such as around 25 August, and at times of wind speed transition, such as near 12 August, the levels in R3 and R4 are higher than expected for the prevailing wind speed. The higher than expected levels near 25 August likely result from obscuration of the signal generated by light local winds by signals from other sources. Note that some short-duration increases in level in R4 appear to correlate with times when wind speed is changing, i.e., short-fetch events. These deviations tend to become smoother above 100 Hz, possibly indicating the frequency where the L-H pressure transitions to other acoustic sources.

6. Conclusions

[78] The 20-month data sets of deep-ocean acoustic pressure, surface wind speed, ocean wave spectra, and seismic spectral time series used in this study provide insight into the pathways and propagation of energy from wind to waves to seismo-acoustic signals in the ocean and solid earth. A summary of findings follows.

[79] The primary source of energy resulting in background acoustic levels at the ocean floor from 0.05 Hz to over 5 kHz at Station ALOHA is wind-forced ocean surface waves.

[80] Acoustic levels below 0.4 Hz (R1) correlate with local wave and seismic spectra but not with local wind speed. The characteristics of these correlations imply that local and distant swell interactions near shorelines and in the deep ocean generate seismic waves that are detected by the hydrophone and seismic stations. Energy below 0.4 Hz is likely dominated by local sources when large local storms are near the islands.

[81] Between 0.4 Hz and approximately 80 Hz, the acoustic spectrum background is the result of the Longuet-Higgins mechanism transmitting local wind-generated ocean surface wave energy to the seafloor from a source region around the hydrophone.

[82] Acoustic spectra at frequencies above 0.4 Hz up to $\hat{f} \sim 5$ (R2) are strongly affected by decreasing directionality of the ocean wavefield with increasing frequency. Near $\hat{f} = 5$ the wavefield directionality appears to approach near-

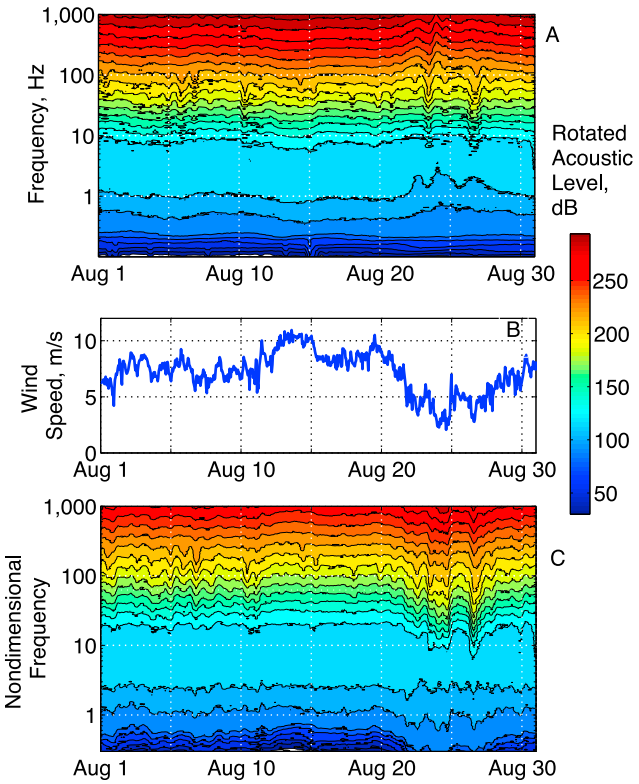

Figure 18. Spectrograms and wind speed time series for August, 2007. The spectral levels have been rotated by f^8 to flatten levels in R3. (a) Spectrogram plotted versus acoustic frequency and (c) spectrogram plotted versus nondimensional frequency. (b) The U_{10} wind speed from the WHOTS buoy. Contour levels are the same in Figures 18a and 18c.

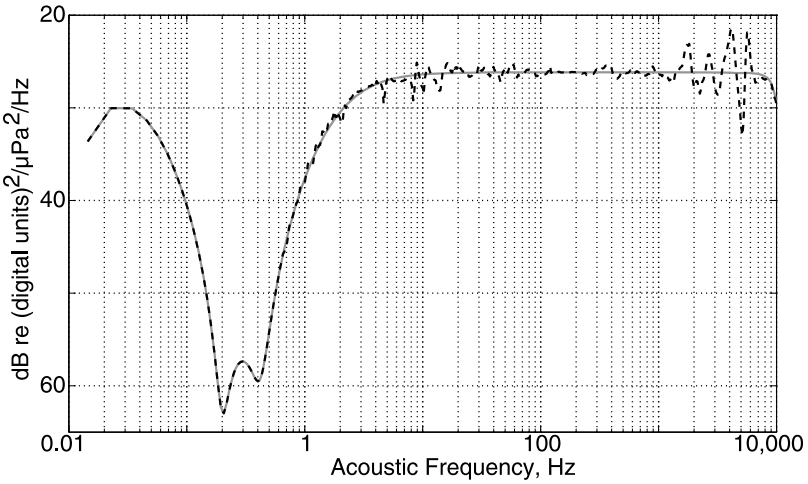

Figure A1. Hydrophone system response (black dashed) and modified response (gray) based on observed narrow-band oscillations.

isotropic conditions, and the overlap integral approaches values near $1/(2\pi)$.

[83] Between $\hat{f}$ = 5 to ~20 (R3) the acoustic spectrum reflects saturation of the nearly isotropic wavefield with an acoustic spectral slope of f^{-8}. Wave theory predicts that the slope of the Longuet-Higgins pressure spectrum should be f^{-7} rather than f^{-8}. This discrepancy may be the result of low-pass filtering by interactions with the ocean floor, by a wave energy spectral slope of $\kappa^{-4.25}$ in the saturated region (rather than the more accepted value of κ^{-4}), by stronger attenuation of the higher frequency seismo-acoustic component of the observed energy, or by some unknown effect.

[84] The change from R3 to R4 is characterized by a sharp break in slope of the acoustic spectrum near $\hat{f}$ = 20, corresponding to a wind speed dependent change of the wave elevation spectrum from $\kappa^{-4.25}$ to κ^{-2} as discussed by *Farrell and Munk* [2008], *Hwang* [2005], and *Elfouhaily et al.* [1997]. At wind speeds below about 5 m/s the join frequency appears to be lower than $\hat{f}$ = 20, but this may be the result of other acoustic sources dominating the acoustic spectrum when wind speeds are low [*Gaul et al.*, 2007].

[85] Above about 80 Hz acoustic frequency, the Longuet-Higgins mechanism and our extended equilibrium wave model predict acoustic levels that are higher than observed unless the secondary peak in the wave elevation curvature spectrum is near κ_m = 250 rpm rather than 370 rpm [*Elfouhaily et al.*, 1997]. The lower value of κ_m may be the result of reduced surface tension by surfactants [*Cox and Munk*, 1954; *Hara and Belcher*, 2002]. Acoustic sources other than the Longuet-Higgins mechanism appear to dominate the acoustic spectrum above about 80 Hz.

[86] Acoustic levels plotted against nondimensional frequency are nearly independent of wind speed from about $1 < \hat{f} < 1000$ for wind speeds above about 5 m/s. Levels are higher than expected when wind speeds are lower and at times when the wind is changing.

[87] The lack of direct measurements of the directional wavefield, particularly above 0.5 Hz, prevents definitive answers to the issues discussed. Future studies involving arrays of broadband hydrophones and seismometers collocated with wind and directional wave buoys should further constrain the relationships discussed in this paper, and enable study of the effects of fetch, wind duration, and the seismic contributions to the acoustic field.

Appendix A

[88] The hydrophone system response, including the amplifier, twin-T pre-whitening filter and hydrophone response [*Duennebier et al.*, 2002], is shown in Figure A1 by the black smooth line. The pre-whitening filter that strongly attenuates the signal in the microseism range (0.1–1 Hz) is an analog filter with a response that could be inaccurate by several dB where attenuation is strongest, thus caution should be exercised when interpreting levels from 0.15 to 0.3 Hz. We have chosen to remove persistent time-independent narrow-band oscillations from the data using the procedure discussed below. The sources of the oscillations below 20 Hz are not associated with wind speed or any other known variable, but they are similar to oscillations predicted for sedimented ocean bottoms [*Kibblewhite and Wu*, 1996; *Stephen et al.*, 2007], and the oscillations above 1 kHz are likely associated with the physical size of the sensor relative to the acoustic wavelength. The removal of these oscillations from the spectra, while not required by the analysis, reduces scatter considerably.

[89] The spectrum consisting of median values of the 11,344 hourly spectral estimates at each of the 474 log-spaced frequencies for the entire 20-month data set was de-trended and high-pass filtered using a zero-phase single-pole filter with a corner at 0.5 Hz. The resulting high-passed spectrum was added to the instrument response yielding the dashed black curve in Figure A1. This curve is then subtracted from the raw data spectra to form the spectra used in this study.

[90] When the ACO was reinstalled in May 2011, the hydrophone was placed within 1 m (rather than 10 m) above the floor where it should be more heavily affected by bottom interactions [*Kibblewhite and Wu*, 1996], and comparisons between the data discussed here and the new data may reflect the change.

[91] **Acknowledgments.** We thank William Farrell, Peter Bromirski, Ralph Stephen, Christine Pequignet and two anonymous reviewers for valuable discussions, and Charles McCreery for valuable discussions and permission to use a figure from his dissertation. Funding for the ALOHA Cabled Observatory was provided by the National Science Foundation and the State of Hawaii through the School of Ocean and Earth Sciences and Technology at the University of Hawaii-Manoa (F. Duennebier, PI). Donations from AT&T and TYCOM and the cooperation of the U.S. Navy made this project possible. The WHOI-Hawaii Ocean Time series Station (WHOTS) mooring is maintained by Woods Hole Oceanographic Institution (PIs R. Weller and A. Plueddemann) with funding from the NOAA Climate Program Office/Climate Observation Division. NSF grant OCE-0926766 supported R. Lukas (co-PI) to augment and collaborate on the maintenance of WHOTS. Lukas was also supported during this analysis by The National Ocean Partnership Program "Advanced Coupled Atmosphere-Wave-Ocean Modeling for Improving Tropical Cyclone Prediction Models" under contract N00014-10-1-0154 to the University of Rhode Island (I. Ginis, PI). The Waimea wave buoy is operated by the University of Hawaii Sea Level Center; buoy data were obtained from the Coastal Data Information Center at the Scripps Institution of Oceanography. The facilities of the IRIS Data Management System, and specifically the IRIS Data Management Center, were used for access to waveform and metadata required in this study. SOEST contribution 8560.

References

Alves, J. H. G. M., M. L. Banner, and I. R. Young (2003), Revisiting the Pierson–Moskowitz asymptotic limits for fully developed wind waves, *J. Phys. Oceanogr.*, *33*, 1301–1323, doi:10.1175/1520-0485(2003)033<1301:RTPALF>2.0.CO;2.

Ardhuin, F., E. Stutzmann, M. Schimmel, and A. Mangeney (2011), Ocean wave sources of seismic noise, *J. Geophys. Res.*, *116*, C09004, doi:10.1029/2011JC006952.

Aucan, J. (2006), Directional wave climatology for the Hawaiian islands from buoy data and the influence of ENSO on extreme wave events from model hindcast, *Tech. Rep., 34*, Jt. World Meteorol. Organ./Int. Oceanogr. Comm. Tech. Comm. for Oceanogr. and Mar. Meteorol., Geneva, Switzerland.

Babcock, J. M., B. A. Kirkendall, and J. A. Orcutt (1994), Relationships between ocean bottom noise and the environment, *Bull. Seismol. Soc. Am.*, *86*(6), 1991–2007.

Banner, M. L. (1990), Equilibrium spectra of wind waves, *J. Phys. Oceanogr.*, *20*, 966–984, doi:10.1175/1520-0485(1990)020<0966:ESOWW>2.0.CO;2.

Banner, M. L., and D. H. Peregrine (1993), Wave breaking in deep water, *Annu. Rev. Fluid Mech.*, *25*, 373–397, doi:10.1146/annurev.fl.25.010193.002105.

Banner, M. L., I. S. F. Jones, and J. C. Trinder (1989), Wavenumber spectra of short gravity waves, *J. Fluid Mech.*, *65*, 647–656, doi:10.1017/S0022112074001583.

Banner, M. L., A. V. Babanin, and I. R. Young (2000), Breaking probability for dominant waves on the sea surface, *J. Phys. Oceanogr.*, *30*, 3145–3160, doi:10.1175/1520-0485(2000)030<3145:BPFDWO>2.0.CO;2.

Bromirski, P. D. (2001), Vibrations from the "Perfect Storm," *Geochem. Geophys. Geosyst.*, *2*(7), 1030, doi:10.1029/2000GC000119.

Bromirski, P. D. (2009), Earth vibrations, *Science*, *324*, 1026–1027, doi:10.1126/science.1171839.

Bromirski, P. D., R. E. Flick, and N. Graham (1999), Ocean wave height determined from inland seismometer data: Implications for investigating wave climate changes in the NE Pacific, *J. Geophys. Res.*, *104*(C9), 20,753–20,766, doi:10.1029/1999JC900156.

Bromirski, P. D., F. K. Duennebier, and R. A. Stephen (2005), Mid-ocean microseisms, *Geochem. Geophys. Geosyst.*, *6*, Q04009, doi:10.1029/2004GC000768.

Carswell, J. R., W. J. Donnely, R. E. McIntosh, M. A. Donelan, and D. C. Vandemark (1999), Analysis of C and Ku band ocean backscatter measurements under low-wind conditions, *J. Geophys. Res.*, *104*, 20,687–20,701, doi:10.1029/1999JC900140.

Cato, D. H. (1991), Theoretical and measured underwater noise from surface wave orbital motion, *J. Acoust. Soc. Am.*, *89*, 1096–1112, doi:10.1121/1.400528.

Cessaro, R. K. (1994), Sources of primary and secondary microseisms, *Bull. Seismol. Soc. Am.*, *84*, 142–148.

Chevrot, S., M. Sylvander, S. Benahmed, C. Ponsolles, J. M. Lefèvre, and D. Paradis (2007), Source locations of secondary microseisms in western Europe: Evidence for both coastal and pelagic sources, *J. Geophys. Res.*, *112*, B11301, doi:10.1029/2007JB005059.

Chi, W. C., W. J. Chen, B. Y. Kuo, and D. Dolenc (2010), Seismic monitoring of western Pacific typhoons, *Mar. Geophys. Res.*, *31*, 239–251, doi:10.1007/s11001-010-9105-x.

Colbo, K., and R. A. Weller (2009), Accuracy of the IMET sensor package in the subtropics, *J. Atmos. Oceanic Technol.*, *26*(9), 1867–1890, doi:10.1175/2009JTECHO667.1.

Cox, C., and W. Munk (1954), Measurement of the roughness of the sea surface from photographs of the Sun's glitter, *J. Opt. Soc. Am.*, *44*, 838–850, doi:10.1364/JOSA.44.000838.

Dahm, T., F. Tillmann, and J. P. Morgan (2006), Seismic broadband ocean-bottom data and noise observed with free-fall stations: Experiences from long-term deployments in the North Atlantic and the Tyrrhenian Sea, *Bull. Seismol. Soc. Am.*, *96*, 647–664, doi:10.1785/0120040064.

Diachok, O., and F. K. Duennebier (2010), Blue whale vocalizations and the seasonal variability of ambient noise levels at the Aloha Observatory, *J. Acousti. Soc. Am.*, *127*(3), 1784.

Donelan, M. A., J. Hamilton, and W. H. Hui (1985), Directional spectra of wind-generated waves, *Philos. Trans. R. Soc. London, Ser. A*, *315*, 509–562, doi:10.1098/rsta.1985.0054.

Donelan, M. A., W. M. Drennan, and K. B. Katsaros (1997), The air-sea momentum flux in conditions of wind sea and swell, *J. Phys. Oceanogr.*, *27*, 2087–2099, doi:10.1175/1520-0485(1997)027<2087:TASMFI>2.0.CO;2.

Duennebier, F. K., D. W. Harris, J. Jolly, J. Babinek, D. Copson, and K. Stiffel (2002), The Hawaii-2 Observatory Seismic System, *IEEE J. Ocean Eng.*, *27*(2), 212–217, doi:10.1109/JOE.2002.1002475.

Duennebier, F., D. Harris, and J. Jolly (2008), ALOHA cabled observatory will monitor ocean in real time, *Sea Technol.*, *49*, 51–54.

Elfouhaily, T., B. Chapron, K. Katsaros, and D. Vandemark (1997), A unified directional spectrum for long and short wind-driven waves, *J. Geophys. Res.*, *102*(C7), 15,781–15,796, doi:10.1029/97JC00467.

Elgar, S., T. H. C. Herbers, and R. T. Guza (1994), Reflection of ocean surface gravity waves from a natural beach, *J. Phys. Oceanogr.*, *24*, 1503–1511, doi:10.1175/1520-0485(1994)024<1503:ROOSGW>2.0.CO;2.

Ewans, K. C. (1998), Observations of the directional spectrum of fetch-limited waves, *J. Phys. Oceanogr.*, *28*, 495–512, doi:10.1175/1520-0485(1998)028<0495:OOTDSO>2.0.CO;2.

Farrell, W. E., and W. Munk (2008), What do deep sea pressure fluctuations tell about short surface waves?, *Geophys. Res. Lett.*, *35*, L19605, doi:10.1029/2008GL035008.

Farrell, W. E., and W. Munk (2010), Booms and busts in the deep, *J. Phys. Oceanogr.*, *40*, 2159–2169, doi:10.1175/2010JPO4440.1.

Forristall, G. Z., and K. C. Ewans (1998), Worldwide measurements of directional wave overlap, *J. Atmos. Oceanic Technol.*, *15*, 440–469, doi:10.1175/1520-0426(1998)015<0440:WMODWS>2.0.CO;2.

Garcés, M. A., C. H. Hetzer, M. Willis, and S. Businger (2003), Integration of infrasonic models with ocean wave spectra and atmospheric specifications to produce estimates of microbarom signal levels, paper presented at 25th Seismic Research Review—Nuclear Explosion Monitoring: Building the Knowledge Base, Natl. Nucl. Security Admin., Tucson, Ariz.

Gaul, R. D., D. P. Knobles, J. A. Shooter, and A. F. Wittenborn (2007), Ambient noise analysis of deep ocean measurements in the northeast Pacific, *IEEE J. Ocean Eng.*, *32*(2), 497–512, doi:10.1109/JOE.2007.891885.

Hara, T., and S. E. Belcher (2002), Wind forcing in the equilibrium range if wind-wave spectra, *J. Fluid Mech.*, *470*, 223–235, doi:10.1017/S0022112002001945.

Hara, T., E. J. Bock, and M. Donelan (1997), Frequency-wavenumber spectrum of wind-generated gravity-capillary waves, *J. Geophys. Res.*, *102*, 1061–1072, doi:10.1029/96JC03229.

Hasselmann, K. (1963), A statistical analysis of the generation of microseisms, *Rev. Geophys.*, *1*, 177–210, doi:10.1029/RG001i002p00177.

Hasselmann, K., et al. (1973), *Measurements of Wind-Wave Growth and Swell Decay During the Joint North Sea Wave Project (JONSWAP)*, *Dtsch. Hydrogr. Z.*, *8*(12), 95 pp.

Hasselmann, K., D. B. Ross, P. Müller, and W. Sell (1976), A parametric wave prediction model, *J. Phys. Oceanogr.*, *6*, 200–228, doi:10.1175/1520-0485(1976)006<0200:APWPM>2.0.CO;2.

Hristov, T., C. Friehe, and S. Miller (1998), Wave-coherent fields in air flow over ocean waves: Identification of cooperative behavior buried in turbulence, *Phys. Rev. Lett.*, *81*, 5245–5248, doi:10.1103/PhysRevLett.81.5245.

Hughes, B. (1976), Estimates of underwater sound (and infrasound) produced by nonlinearly interacting ocean waves, *J. Acoust. Soc. Am.*, *60*(5), 1032–1038, doi:10.1121/1.381203.

Hwang, P. A. (1997), A study of the wavenumber spectra of short water waves in the ocean. Part II: Spectral model and mean square slope, *J. Atmos. Oceanic Technol.*, *14*, 1174–1186, doi:10.1175/1520-0426(1997)014<1174:ASOTWS>2.0.CO;2.

Hwang, P. A. (2005), Wave number spectrum and mean square slope of intermediate-scale ocean surface waves, *J. Geophys. Res.*, *110*, C10029, doi:10.1029/2005JC003002.

Hwang, P. A. (2008), Observations of swell influence on ocean surface roughness, *J. Geophys. Res.*, *113*, C12024, doi:10.1029/2008JC005075.

Hwang, P. A., and D. W. Wang (2001), Directional distributions and mean square slopes in the equilibrium and saturation ranges of the wave spectrum, *J. Phys. Oceanogr.*, *31*, 1346–1360, doi:10.1175/1520-0485(2001)031<1346:DDAMSS>2.0.CO;2.

Hwang, P. A., and D. W. Wang (2004), An empirical investigation of source term balance of small scale surface waves, *Geophys. Res. Lett.*, *31*, L15301, doi:10.1029/2004GL020080.

Janssen, P. A. E. M., H. Wallbrink, C. J. Calkoen, D. van Halsema, W. A. Oost, and P. Snoeij (1998), Viers-1 scatterometer model, *J. Geophys. Res.*, *103*, 7807–7831, doi:10.1029/97JC02911.

Karl, D. M., and R. Lukas (1996), The Hawaii Ocean Time-series (HOT) program: Background, rationale and field implementation, *Deep Sea Res., Part II*, *43*, 129–156, doi:10.1016/0967-0645(96)00005-7.

Kedar, S., M. Longuet-Higgins, F. Webb, N. Graham, R. Clayon, and C. Jones (2008), The origin of deep-ocean microseisms in the North Atlantic Ocean, *Proc. R. Astron. Soc. A*, *464*, 777–793, doi:10.1098/rspa.2007.0277.

Kerman, B. R. (1984), Underwater sound generation by breaking waves, *J. Acoust. Soc. Am.*, *75*, 149–165, doi:10.1121/1.390409.

Kibblewhite, A. C., and C. Y. Wu (1991), The theoretical description of wave-wave interactions as a noise source in the ocean, *J. Acoust. Soc. Am.*, *89*, 2241–2252, doi:10.1121/1.400970.

Kibblewhite, A. C., and C. Y. Wu (Eds.) (1996), *Wave Interactions as a Seismo-acoustic Source*, Springer, Berlin, doi:10.1007/BFb0011210.

Kudryavtsev, V., and J. Johannessen (2004), On effect of wave breaking on short wind waves, *Geophys. Res. Lett.*, *31*, L20310, doi:10.1029/2004GL020619.

Kudryavtsev, V., and V. K. Makin (2002), Coupled dynamics of short waves and the airflow over long surface waves, *J. Geophys. Res.*, *107*(C12), 3209, doi:10.1029/2001JC001251.

Kudryavtsev, V., V. K. Makin, and B. Chapron (1999), Coupled sea surface-atmosphere model: 2. Spectrum of short wind waves, *J. Geophys. Res.*, *104*, 7625–7639, doi:10.1029/1999JC900005.

Liu, Y., and X.-H. Yan (1995), The wind-induced wave growth rate and the spectrum of the gravity-capillary waves, *J. Phys. Oceanogr.*, *25*, 3196–3218, doi:10.1175/1520-0485(1995)025<3196:TWIWGR>2.0.CO;2.

Longuet-Higgins, M. S. (1950), A theory of microseisms, *Philos. Trans. R. Soc. London, Ser. A*, *243*, 1–35, doi:10.1098/rsta.1950.0012.

Ma, B. B., J. A. Nystuen, and R.-C. Lien (2005), Prediction of underwater sound levels from rain and wind, *J. Acoust. Soc. Am.*, *117*, 3555–3565, doi:10.1121/1.1910283.

McCreery, C. S. (1992), Long-term ambient ocean noise, 0.05–30 Hz, from the Wake Island hydrophone array, PhD thesis, Dep. of Geol. and Geophys., Univ. of Hawai'i at Mānoa, Honolulu.

McCreery, C. S., F. K. Duennebier, and G. H. Sutton (1993), Correlation of deep ocean noise (0.4–30 Hz) with wind, and the Holu Spectrum—A worldwide constant, *J. Acoust. Soc. Am.*, *93*, 2639–2648, doi:10.1121/1.405838.

Melville, W. K. (1996), The role of surface-wave breaking in air-sea interaction, *Annu. Rev. Fluid Mech.*, *28*, 279–321, doi:10.1146/annurev.fl.28.010196.001431.

Melville, W. K., and P. Matusov (2002), Distribution of breaking waves at the ocean surface, *Nature*, *417*, 58–63, doi:10.1038/417058a.

Mitsuyasu, H., F. Tasai, T. Suhara, S. Mizuno, M. Ohkusu, T. Honda, and K. Rikushi (1975), Observations of the directional spectrum of ocean waves using a cloverleaf buoy, *J. Phys. Oceanogr.*, *5*, 750–760, doi:10.1175/1520-0485(1975)005<0750:OOTDSO>2.0.CO;2.

Mueller, J. A., and F. Veron (2009), Nonlinear formulation of the bulk surface stress over breaking waves: Feedback mechanisms from air-flow separation, *Boundary Layer Meteorol.*, *130*, 117–134, doi:10.1007/s10546-008-9334-6.

Munk, W. (2009), An inconvenient sea truth: Spread, steepness, and skewness of surface slopes, *Annu. Rev. Mar. Sci.*, *1*, 377–415, doi:10.1146/annurev.marine.010908.163940.

Phillips, O. M. (1958), The equilibrium range in the spectrum of wind-generated waves, *J. Fluid Mech.*, *4*, 426–434, doi:10.1017/S0022112058000550.

Phillips, O. M. (1985), Spectral and statistical properties of the equilibrium range in wind-generated gravity waves, *J. Fluid Mech.*, *156*, 505–531, doi:10.1017/S0022112085002221.

Pierson, W. J. (1982), The Spectral Ocean Wave Model (SOWM), a northern hemisphere computer model for specifying and forecasting ocean wave spectra, *Final Rep., DlNSRDC-82/11*, U.S. Nav. Oceanogr. Command Detachment, Asheville, N. C.

Pierson, W. J., and L. Moskowitz (1964), A proposed spectral form for fully developed wind seas based on the similarity theory of S. A. Kitaigorodskii, *J. Geophys. Res.*, *69*, 5181–5190, doi:10.1029/JZ069i024p05181.

Plueddemann, A. J., R. A. Weller, R. Lukas, J. Lord, P. R. Bouchard, and M. A. Walsh (2006), WHOI Hawaii Ocean Timeseries Station (WHOTS): WHOTS-2 mooring turnaround cruise report, *Tech. Rep., WHOI-2006-08*, Woods Hole Oceanogr. Inst., Woods Hole, Mass.

Resio, D. T., C. E. Long, and W. Perrie (2011), The role of nonlinear momentum fluxes on the evolution of directional wind-wave spectra, *J. Phys. Oceanogr.*, *41*, 781–801, doi:10.1175/2010JPO4545.1.

Rozenberg, A., and M. Ritter (2005), Laboratory study of the fine structure of short surface waves due to breaking: Two-directional wave propagation, *J. Geophys. Res.*, *110*, C02011, doi:10.1029/2004JC002396.

Stephen, R. A., P. D. Bromirski, and F. K. Duennebier (2007), The effects of local structure on seafloor ambient noise at the Hawaii-2 Observatory, in *Symposium on Underwater Technology and Workshop on Scientific Use of Submarine Cables and Related Technologies*, pp. 605–611, Inst. of Electr. and Electron. Eng., New York.

Sutton, G. H., and N. Barstow (1990), Ocean-bottom ultralow-frequency (ULF) seismo-acoustic ambient noise: 0.002 to 0.4 Hz, *J. Acoust. Soc. Am.*, *87*(5), 2005–2012, doi:10.1121/1.399328.

Toffoli, A., M. Onorato, E. M. Bitner-Gregersen, and J. Monbaliu (2010), Development of a bimodal structure in ocean wave spectra, *J. Geophys. Res.*, *115*, C03006, doi:10.1029/2009JC005495.

Traer, J., P. Gerstoft, P. D. Bromirski, W. S. Hodgkiss, and L. A. Brooks (2008), Shallow-water seismoacoustic noise generated by tropical storms Ernesto and Florence, *J. Acoust. Soc. Am.*, *124*(3), 170–176, doi:10.1121/1.2968296.

Tsai, W., and N.-L. Liu (2003), An assessment of the effect of sea surface surfactant on global atmosphere-ocean CO_2 flux, *J. Geophys. Res.*, *108*(C4), 3127, doi:10.1029/2000JC000740.

Wang, D. W., and P. A. Hwang (2001), Evolution of the bimodal directional distribution of ocean waves, *J. Phys. Oceanogr.*, *31*, 1200–1221, doi:10.1175/1520-0485(2001)031<1200:EOTBDD>2.0.CO;2.

Webb, S. C. (2007), The Earth's 'hum' is driven by ocean waves over the continental shelves, *Nature*, *445*, 754–756, doi:10.1038/nature05536.

Webb, S. C., and C. S. Cox (1986), Observations and modeling of seafloor microseism, *J. Geophys. Res.*, *91*(B7), 7343–7358, doi:10.1029/JB091iB07p07343.

Webb, S. C., and A. Schultz (1992), Very low frequency ambient noise at the seafloor under the Beaufort Sea icecap, *J. Acoust. Soc. Am.*, *91*, 1429–1439, doi:10.1121/1.402474.

Wilcock, W. S. D., S. C. Webb, and I. T. Bjarnason (1999), The effect of local wind on seismic noise near 1 Hz at the MELT site and in Iceland, *Bull. Seismol. Soc. Am.*, *89*, 1543–1557.

Xiradakis, P. (2009), The refractive effects of laser propagation through the ocean and within the ocean, M.S. thesis, Nav. Postgrad. Sch., Monterey, Calif.

Yarin, A. L. (2006), Drop impact dynamics: Splashing, spreading, receding, bouncing…, *Annu. Rev. Fluid Mech.*, *38*, 159–192, doi:10.1146/annurev.fluid.38.050304.092144.

Zhang, J., P. Gerstoft, and P. Bromirski (2010), Pelagic and coastal sources of P wave microseisms: Generation under tropical cyclones, *Geophys. Res. Lett.*, *37*, L15301, doi:10.1029/2010GL044288.

J. Aucan, Laboratoire d'Etudes en Géophysique et Océanographie Spatiale, Institut de Recherche pour le Développement, 14 Av. Edouard Belin, F-31400 Toulouse, France. (jerome.aucan@legos.obs-mip.fr)

F. K. Duennebier, Department of Geology and Geophysics, SOEST, University of Hawai'i at Mānoa, Honolulu, HI 96822, USA. (fred@soest.hawaii.edu)

R. Lukas, Department of Oceanography, SOEST, University of Hawai'i at Mānoa, Honolulu, HI 96822, USA. (rlukas@hawaii.edu)

E.-M. Nosal, Department of Ocean Resources and Engineering, SOEST, University of Hawai'i at Mānoa, Honolulu, HI 96822, USA. (nosal@hawaii.edu)

R. A. Weller, Woods Hole Oceanographic Institution, 266 Woods Hole Rd., MS 29, Woods Hole, MA 02543-1050, USA. (rweller@whoi.edu)